Multifactorial stroma-mediated resistance is a major contributor to residual disease under targeted therapies in lung cancers

Andriy Marusyk

andriy.marusyk@moffitt.org

H. Lee Moffitt Cancer Center & Research Institute   https://orcid.org/0000-0002-0087-9575

Bina Desai

H. Lee Moffitt Cancer Center & Research Institute

Tatiana Miti

H. Lee Moffitt Cancer Center & Research Institute

Sandhya Prabhakaran

H. Lee Moffitt Cancer Center & Research Institute

Daria Miroshnychenko

H. Lee Moffitt Cancer Center & Research Institute

Menkara Henry

H. Lee Moffitt Cancer Center & Research Institute

Viktoriya Marusyk

H. Lee Moffitt Cancer Center & Research Institute

Pragya Kumar

H. Lee Moffitt Cancer Center & Research Institute

Hilal Ozakinci

H. Lee Moffitt Cancer Center & Research Institute

Chandler Gatenbee

H. Lee Moffitt Cancer Center & Research Institute   https://orcid.org/0000-0002-9730-5964

Marilyn Bui

Moffitt Cancer Center   https://orcid.org/0000-0003-4963-2255

Theresa Boyle

Moffit   https://orcid.org/0000-0001-5950-3970

Jacob Scott

Cleveland Clinic   https://orcid.org/0000-0003-2971-7673

Philipp Altrock

Max Planck Institute for Evolutionary Biology   https://orcid.org/0000-0001-7731-3345

Eric Haura

Moffitt Cancer Center

Alexander Anderson

H. Lee Moffitt Cancer Center & Research Institute   https://orcid.org/0000-0002-2536-4383

David Basanta

Article

Keywords:

Additional Declarations: There is **NO** Competing Interest.

Multifactorial stroma-mediated resistance is a major contributor to residual disease under targeted therapies in lung cancers.

Authors: Bina Desai[1,2], Tatiana Miti[3], Sandhya Prabhakaran[3], Daria Miroshnychenko[1], Menkara Henry[1], Viktoriya Marusyk[1], Pragya Kumar[1], Hilal Ozakinci[4], Chandler Gatenbee[3], Marilyn Bui[5,6], Theresa A. Boyle[4,5], Jacob Scott[7], Philipp M. Altrock[8], Eric Haura[4], Alexander R.A. Anderson[3], David Basanta[3], Andriy Marusyk[1,9]*.

Affiliations:

[1]Department of Tumor Microenvironment and Metastasis, H Lee Moffitt Cancer Centre and Research Institute; Tampa, FL, USA.

[2]Cancer Biology Ph.D. Program, University of South Florida; Tampa, FL, USA.

[3]Department of Integrated Mathematical Oncology, H Lee Moffitt Cancer Center and Research Institute; Tampa, FL, USA.

[4]Department of Thoracic Oncology, H. Lee Moffitt Cancer Center and Research Institute; Tampa, FL, USA.

[4]Department of Pathology, H. Lee Moffitt Cancer Center and Research Institute; Tampa, FL, USA.

[5]Department of Machine Learning, H. Lee Moffitt Cancer Center and Research Institute; Tampa, FL, USA.

[7]Department of Translational Hematology and Oncology Research, Cleveland Clinic; Cleveland, OH, USA.

[8]Department of Theoretical Biology, Max Planck Institute for Evolutionary Biology; Ploen, Germany.

[9]Department of Molecular Medicine, University of South Florida; Tampa, FL, USA.

23 *Corresponding author. Email: andriy.marusyk@moffitt.org

24 **One Sentence Summary:** Peristromal niches protect lung cancer cells from therapeutic

25 elimination and contribute to relapse through a combination of multiple molecular mechanisms.

26 **Abstract:** Despite inducing strong and durable clinical responses, targeted therapies do not

27 eliminate advanced cancers, as a subset of tumor cells survives within residual tumors, eventually

28 developing resistance. The ability of tumor cells to avoid therapeutic elimination can be mediated

29 both by cell-intrinsic and microenvironmental mechanisms. Whilst the specific molecular

30 mediators of cell-intrinsic and microenvironmental resistance are well understood, their relative

31 contribution to *in vivo* therapeutic responses remains poorly defined. Using spatial histological

32 inferences from experimental models of ALK+ NSCLC, we found that peristromal niches

33 protected tumor cells from therapeutic elimination in vivo, enabling in vivo persistence. Whereas

34 the development of bona fide resistance is associated with the development of the development of

35 cell-intrinsic resistance, relapse of tumor growth reflects a combined effect of both cell-intrinsic

36 and microenvironmental mechanisms. Mechanistically, the protective effect of the peristromal

37 niche is not reducible to a single mechanism, instead reflecting a combined effect of multiple

38 juxtacrine and paracrine mediators. The lack of reducibility to a single molecular mediator presents

39 an obvious challenge to the therapeutic paradigms of targeting individual resistance mechanisms.

40 We found that this challenge could be mitigated by shifting the therapeutic focus to orthogonal

41 collateral sensitivities of residual tumors. Exploiting adaptive upregulation of HER2, associated

42 with both cell-intrinsic and microenvironmental persistence, using the antibody-drug conjugate T-

43 DXd strongly enhanced the effect of targeted therapies and suppressed the development of

44 resistance.

45

INTRODUCTION

Therapies that target oncogenic signaling addictions can induce strong and durable remissions in cancers defined by relevant mutational drivers. However, a subset of tumor cells typically persists under therapy, eventually giving rise to resistance. The main effort in the quest to solve the challenge of the inevitable failure of targeted therapies has been directed against the identification and targeting of the molecular mechanisms that underlie cancer survival (persistence) and resistance (positive net growth). This effort has led to the uncovering of a large and growing number of molecular mechanisms, including mutational changes in therapeutic targets, mutational or non-mutational activation of bypass signaling, histological transformation, and others (1). However, apart from the improvements that stem from overcoming the effects of common on-target mutations through improved inhibitor design, our knowledge of resistance mechanisms has not translated into therapeutic advances.

To a large extent, this paucity in therapeutic advances stems from intra-tumor heterogeneity of resistance mechanisms (2). When subpopulations with different resistance mechanisms are present at relapse, suppression or elimination of the dominant subpopulation cannot be expected to yield more than a temporary effect. A less appreciated but likely equally important issue is that, even at the level of individual tumor cells, therapeutic resistance can result from a combined effect of multiple mechanisms (3-5). Subsequently, suppressing one of the mechanisms within a compound resistance scenario does not lead to a full re-sensitization. Finally, therapy resistance is not limited to cell-intrinsic sources. A large body of experimental evidence points to contribution from the tumor microenvironment (TME), as paracrine and juxtacrine factors produced by tumor stroma are known to confer therapy resistance to otherwise sensitive tumor cells (6-8). These effects, which we describe under the umbrella term of stroma-mediated (SM) resistance (SMR), have been

69 well-documented across various therapeutic contexts but appear to be particularly relevant for

70 targeted therapies directed against oncogenic signaling addictions, such as inhibitors of EGFR and

71 ALK mutations in non-small cell lung cancers (NSCLC). While specific cases of experimental or

72 clinical relapse are typically attributed to a single dominant mechanism, either cell-intrinsic or

73 stroma-mediated, this attribution is likely an oversimplification. Common experimental models of

74 targeted therapy sensitivity are typically capable of developing therapy resistance under stroma-

75 free *in vitro* culture conditions (3,5,9-11). Yet, the same experimental models can be rendered

76 partially or fully therapy-resistant by co-culture with either cancer-associated fibroblasts (CAFs)

77 (the main cellular component of TME), CAF conditioned media (CM), or specific CAF-produced

78 cytokines, extracellular matrix (ECM) components, and other CAF-produced factors (8,12,13).

79 Therefore, *in vivo,* therapeutic responses could be expected to reflect a combined contribution of

80 both cell-intrinsic resistance and SMR mechanisms.

81 Uncovering the relative contribution of cell-intrinsic resistance and SMR to *in vivo* therapeutic

82 responses could be potentially achieved by disabling one of them and examining the resulting

83 effect on therapeutic responses in experimental animal models. Whereas cell-intrinsic therapy

84 resistance is typically attributed to a single mutational or non-mutational mechanism, our studies

85 with experimental models of ALK+ NSCLC revealed a more complex scenario of multifactorial

86 resistance (5). Subsequent work of Franca et al. indicated a wide generalizability of this

87 multifactorial underpinning, proposing the concept of a "resistance continuum"(3). Since the

88 multifactorial underpinning of cell-intrinsic resistance limits its experimental disabling, we

89 decided to focus on identifying and suppressing the molecular mediator of SMR. Given the major

90 role of CAFs in mediating SMR across different contexts of targeted therapies (14-16), we

91 reasoned that an experimental uncoupling of cell-intrinsic resistance and SMR effects might be

92   achievable by identifying and disabling the mechanism(s) responsible for the resistance-conferring

93   effects of CAFs. However, we found that, even at the level of a single experimental model, *in vivo*

94   SMR cannot be reduced to a single molecular mediator. Instead, it reflects a combined effect of

95   multiple juxtacrine and paracrine mechanisms, whose relative contribution changes over the

96   course of therapy. Using spatial analyses of histological samples, we found that SMR plays a

97   dominant role in the ability of tumors to persist and avoid therapeutic elimination. Whereas the

98   relative contribution of SMR diminishes with the transition from remission to the resumption of

99   tumor growth, our analyses indicate that tumor relapse integrates the effects of cell-intrinsic

100   resistance and SMR mechanisms. The complex, multifactorial underpinning of therapeutic

101   responses poses a major challenge to the efforts to overcome therapy resistance. We found that

102   shifting focus from individual resistance mechanisms towards orthogonal therapeutic sensitivities

103   of tumor cells within residual disease and using combination therapies that utilize the bystander

104   effects of antibody-drug conjugates offers a promising solution to the challenges faced by precision

105   oncology.

106   **RESULTS**

107   **Stromal fibroblasts reduce sensitivity of NSCLC cells to targeted therapies via HGF-cMET**

108   **axis *in vitro***

109   To assess the contribution of SMR towards *in vivo* therapeutic responses, we chose to focus on a

110   common experimental model of ALK+ NSCLC, H3122 cell line. ALK+ NSCLC to ALK can be

111   viewed as a "poster child" of both the success and limitations of targeted therapies. While ALK

112   inhibitors typically induce strong and often durable clinical responses, acquired resistance remains

113   unavoidable in advanced metastatic ALK+ NSCLC. Similar to many other experimental models

114   of different contexts of targeted therapies, H3122 cultures can persist under therapy, withstanding

115 therapeutic elimination and eventually developing resistance through cell-intrinsic mechanisms

116 (5). At the same time, ALKi sensitivity of H3122 cells can be greatly reduced in the presence of

117 CAFs (15-19). To dissect the relative contribution of cell-intrinsic, stroma-mediated persistence

118 and resistance to *in vivo* responses to ALKi, we sought to uncouple them by identifying molecular

119 mediator(s) of SMR *in vitro* and examining the effect of its suppression *in vivo*.

120 Consistent with our previous work, co-culture with a primary, non-immortalized lung cancer CAF

121 isolate (subsequently referred to as CAF1) (17) substantially reduced the sensitivity of H3122 to

122 the frontline ALKi alectinib (**Fig. 1A**). CAF1 CM fully phenocopied the effect of a physical CAF1

123 co-culture, indicating that the protective effect is mediated by a secreted factor(s) (**Fig. 1A**). CAF1

124 CM conferred similarly strong protection to clinically approved ALK inhibitors lorlatinib, ceritinib

125 and brigatinib, but not to crizotinib, which co-inhibits cMET (**Fig. 1B**). A similar effect was

126 observed in a different model of ALK+ NSCLC, the STE-1 cell line (**Fig. S1A**). Indicative of the

127 generalizability of these observations towards other targeted therapies in NSCLC, CAF1 CM

128 conferred strong protection against EGFR inhibitors gefitinib and erlotinib in the PC9 cell line

129 model of EGFR mutant NSCLC, capable of cell-intrinsic persistence and resistance (9,11,20) (**Fig.**

130 **S1B**) as well as against KRAS^{G12C} inhibitors sotorasib and ARS-1620 in the H358 model of

131 KRAS^{G12C} NSCLC (**Fig. S1C**). Next, given the known phenotypic diversity of fibroblasts(16,21),

132 we examined the effect CM from a panel of primary human NSCLC CAF isolates as well as

133 fibroblasts isolated from normal lung tissue (NF) (**Fig. S1D**). Despite a variability in the magnitude

134 of the effect, CM from most fibroblast isolates protected H3122 cells against alectinib, lorlatinib,

135 ceritinib, and brigatinib, while having little to no protection against crizotinib (**Fig. 1C**).

136 The lack of protection against crizotinib suggested mediation by the well-established bypass

137 signaling mechanism, activation of cMET expressed by tumor cells by hepatocyte growth factor

138   (HGF), produced by CAFs (15,18,22). Indeed, exogenous HGF conferred strong dose-dependent

139   protection against alectinib in H3122 and STE-1 models (**Fig. S2A, B**). Exogenous HGF, added

140   at the concentrations detected in CAF1 CM (2 ng/ml), fully phenocopied the protective effect of

141   CAF1 CM against alectinib and lorlatinib (**Fig. 1D, S2C**), while providing no detectable protection

142   against crizotinib (**Fig. S2C**). Importantly, we observed a strong correlation (R^2=0.73) between

143   HGF concentration in the CM of different fibroblast isolates and the magnitude of their protection

144   for H3122 cells against alectinib (**Fig 1E**), indicating a generalizability of the CAF1 CM inferences

145   toward other fibroblast isolates. Consistent with the central role of the HGF-cMET axis in

146   mediating the effects of CAFs, the addition of an HGF-neutralizing antibody strongly suppressed

147   the protective effects of CAF CM in H3122 and STE-1 models (**Fig. S2D, E**). Similarly, cMET

148   inhibitors cabozantinib and capmatinib completely suppressed CAF-mediated protection in

149   experimental models of ALK+, EGFR mutant, and KRAS^{G12C} NSCLC (**Fig. 1F, S2F-I**).

150   Importantly, protection observed in short-term growth assays translated into longer-term

151   protection in clonogenic assays (**Fig. 1G, Fig. S2J**). In summary, the substantial reduction of

152   ALKi sensitivity of H3122 cells in the presence of fibroblast CM reflects a general phenomenon

153   of CAF-mediated targeted therapy resistance. At least *in vitro*, the protective effect of CAFs on

154   ALKi sensitivity in the H3122 model can be largely reduced to the well-characterized HGF-cMET

155   bypass signaling mechanism.

156   **Modulation of the HGF-cMET axis moderately impacts alectinib responses *in vivo***

157   Assuming the mechanisms mediating the effect of CAFs are conserved between *in vitro* and *in*

158   *vivo* contexts, the contribution of SMR to alectinib responses of H3122 tumors *in vivo* should be

159   assessable by experimental manipulation of the HGF-cMET axis in xenograft models. However,

160   murine HGF (mHGF) does not activate human cMET(23) (**Fig. S3A**), complicating the assessment

161 and suggesting that SMR might be irrelevant for ALKi responses in conventional murine

162 xenograft models.

163 To overcome this limitation, we first evaluated the ability of human HGF (hHGF) to confer *bona*

164 *fide* resistance *in vivo*. To this end, we overexpressed hHGF in H3122 cells using a lentiviral vector

165 and compared alectinib responses between NSG xenograft tumors formed by subcutaneous grafts

166 of H3122 parental cells, lacking detectable HGF expression and their hHGF overexpressing

167 counterparts. Whereas hHGF expression had no discernable impact on the baseline tumor growth,

168 it prevented tumor regression in response to alectinib (**Fig. 2A, S3B**), indicating that the HGF-

169 cMET axis represents a strong resistance mechanism. However, the observation of the autocrine

170 hHGF-mediated resistance does not directly address the question of the impact of the stroma-

171 produced HGF, as the paracrine-acting effects of SMR mediators might be spatially limited (24).

172 Therefore, to evaluate the impact of the HGF-conferred SMR more directly, we sought to leverage

173 the full compatibility between human HGF and murine cMET; a replacement of both murine HGF

174 alleles in the NSG mice with their human counterparts produces no detectable phenotype, apart

175 from modulating responses of hHGF-responsive human xenografts (25). We reasoned that

176 contrasting therapy responsiveness of parental H3122 cells grafted in the regular NSG strain versus

177 its humanized derivate (NSG^hHGF) should provide a "clean" test of the impact of SMR on

178 therapeutic responses (**Fig. 2B**).

179 Consistent with the lack of impact of HGF on the baseline proliferation of H3122 cells both *in*

180 *vitro* (**Fig. 1D**) and *in vivo* (**Fig. 2A**), we observed no discernable differences in tumor implantation

181 efficiency and baseline tumor growth (**Fig. 2C, S3C, D**). Surprisingly, initial tumor responses to

182 alectinib were indistinguishable between the two mouse models. A moderate reduction of alectinib

183 sensitivity in tumors grafted in NSG^hHGF mice was only detectable at relapse (**Fig. 2C, S3D, E**).

184 To further characterize the impact of the HGF-cMET axis on *in vivo* alectinib sensitivities, we

185 assessed the ability of a highly specific cMET inhibitor, capmatinib, to abrogate the effect of

186 hHGF. (**Fig. 2D**). Given the relatively modest differences between the two models, we used a

187 slightly lower alectinib dosing (20 mg/kg instead of 25 mg/kg) to enhance the ability to detect the

188 effect of the HGF-cMET axis modulation. Consistent with the inability of mHGF to activate

189 human cMET, capmatinib had no discernable effect on the alectinib response of H3122 tumors

190 grafted into NSG mice. In contrast, in NSG^hHGF H3122 xenografts, capmatinib substantially

191 enhanced the magnitude of tumor regression and delayed the relapse (**Fig. 2E, S3F, G**), supporting

192 the relevance of the HGF-cMET axis for stroma-mediated resistance *in vivo.*

193 **Proximity to stroma reduces alectinib sensitivity *in vivo* through a combination of HGF-**

194 **dependent and independent mechanisms**

195 Given the strong effect of ectopic HGF expression *in vivo* (**Fig. 2A**) and the ability of fibroblast-

196 produced HGF to provide ALKi protection *in vitro* (**Fig. 1**), we reasoned that the modest effect of

197 stromal hHGF in xenograft models could reflect the spatial limitations, as cMET activation can be

198 expected to be limited to tumor cells in the immediate proximity to hHGF-producing stroma. To

199 address this possibility, we examined the spatial distribution of tumor cell proliferation in the two

200 xenograft models, using IHC staining of tumor tissue for BrdU, which marks cells undergoing

201 DNA replication. Without treatment, the distribution of BrdU+ cells in tumors collected from

202 animals pulsed with BrdU prior to euthanasia appeared to be random in both the NSG and NSG^hHGF

203 xenograft tumors (**Fig. 2F,** baseline). Consistent with the therapy-protecting effects of CAFs *in*

204 *vitro*, while alectinib treatment potently suppressed cell proliferation, BrdU+ cells could still be

205 observed in the peristromal niches (**Fig. 2F,** remission). Unexpectedly, this effect was detected in

206 both xenograft tumor models, indicating the action of HGF-independent SMR mechanism(s) that

207 overshadow the effects of the HGF-cMET axis (**Fig. 2F**). Tumor relapse was associated with a

208 partial restoration of tumor cell proliferation. Consistent with the reduction in cell-intrinsic ALKi

209 sensitivity, the bias in cell proliferation toward peristromal niches was diminished. However, it

210 has not completely disappeared (**Fig. 2F,** relapse), indicating that the tumor relapse is driven by a

211 combination of both cell-intrinsic and SMR effects.

212 The bias in tumor cell proliferation toward peristromal niches under ALKi therapy was not limited

213 to alectinib treatment, as lorlatinib induced a similar effect in H3122 tumors grafted in regular

214 NSG mice that lacked the functional HGF-cMET axis (**Fig. S4A**). Moreover, the effect was

215 observed in additional experimental models of ALK+ NSCLC. Similar to the H3122 tumors, in

216 the absence of therapy, the distribution of BrdU+ cells appeared random in the NSG xenografts of

217 STE-1, H2228, and MGH006-1 tumors (**Fig. S4B-D**). Alectinib treatment strongly suppressed

218 proliferation, inducing bias in the distribution of BrdU+ cells towards the ECM-rich stroma (**Fig.**

219 **S4B-D**), suggesting the broad generalizability of the SMR. Importantly, IHC staining for a

220 common proliferation marker Ki67 revealed a similar ALKi-induced stroma proximity bias in cell

221 proliferation in clinical samples (**Fig. 2G, Fig. S5**). These observations suggest the following

222 conceptual model (**Fig. 2H**): suppression of oncogenic addiction by targeting therapies suppresses

223 proliferation and induces cell death. However, intrinsically therapy-sensitive cells within

224 peristromal niches are partially protected from these effects. Thus, SMR might represent the major

225 source of in vivo persistence. The SMR protected cells eventually develop partial cell-intrinsic

226 resistance, enabling their proliferation and survival outside of the peristromal niche. However,

227 their proliferation might still be boosted by paracrine signals produced by stroma.

228 To quantitatively assess the impact of stroma proximity on tumor cell proliferation and to evaluate

229 the relative contribution of the HGF-cMET axis, we took advantage of our digital pathology/spatial

230   analysis pipeline (26). In this approach, scanned microscopy images of the anti-BrdU IHC-stained

231   histological tumor cross-sections are segmented into necrotic areas (excluded from the analyses),

232   stromal regions, BrdU+, and BrdU- tumor cells. Continuous stromal regions, defined by clearly

233   distinguishable ECM deposition, are further rasterized to facilitate quantitation (**Fig. 3A**).

234   Our ability to draw accurate quantitative inferences from spatial distributions requires adequate

235   controls. Since therapy reduces the tumor/stroma ratio and alters the relative distribution of tumor

236   parenchyma and stroma, direct comparisons between the control and alectinib-treated tumors are

237   not easily interpretable. To overcome this limitation, the spatial distributions of BrdU+ tumor cells

238   were compared to their sample-specific digital "avatars". These digital avatars retain specific

239   spatial locations of each tumor cell and stromal regions, but the BrdU positivity status is randomly

240   redistributed among the tumor cells while preserving the BrdU+ fraction (**Fig. 3A**). Comparison

241   between the observed and predicted random distributions enables accurate assessment of the

242   spatial proliferation bias in each sample. Comparisons of pairwise (observed versus predicted

243   random) differences between vehicle control and alectinib-treated groups enable the assessment

244   of the impact of therapy. Finally, comparisons of the predicted/observed differences between the

245   NSG and NSGhHGF xenograft tumors enable the assessment of the impact of stromal HGF.

246   Importantly, our pipeline analyses all tumor cells within the histological cross-sections (80K-400K

247   per tumor), with multiple independent tumors analyzed per time point, thus minimizing the impacts

248   of spatial heterogeneity and sampling biases.

249   To assess the impact of stroma proximity on cell proliferation, we assessed the distributions of

250   distances of BrdU+ tumor cells to the nearest stroma (24,27) (**Fig. 3B**), with the predicted random

251   distributions serving as sample-specific null hypothesis controls. Our analyses confirmed the

252   visual inferences of the lack of spatial bias in NSG and NSGhHGF xenograft tumors in the absence

253 of therapy (**Fig. 3C-E**). In contrast, we detected a strong spatial bias in BrdU+ tumor cells towards

254 peri-stromal regions in alectinib-treated tumors. While this bias was most pronounced in

255 regressing tumors, it was also present upon relapse (**Fig. 3C-E**). Consistent with the lack of

256 detectable HGF-dependence on the initial tumor responses (**Fig. 2C**), we did not detect differences

257 in the stroma proximity bias between the NSG and NSG^{hHGF} tumors during remission. However,

258 at relapse, the bias was significantly stronger in the NSG^{hHGF} xenografts (**Fig. 3C-E**), consistent

259 with the divergence of volumetric responses (**Fig.2C**). Taken together, our spatial analyses support

260 the notion that stroma-mediated resistance contributes to both incomplete tumor responses and

261 tumor growth relapse, and indicate that, *in vivo*, stroma-mediated resistance cannot be reduced to

262 the effects of the HGF-cMET axis alone.

263 To uncover the identity of the HGF-independent SMR mechanism(s), we performed

264 transcriptomic analyses of treatment-naïve and alectinib-treated (2 and 6 weeks) tumors from the

265 H3122 NSG and H3122 NSG^{hHGF} xenograft models using bulk Illumina RNA sequencing. Reads

266 were mapped to both human and murine genomes, enabling simultaneous assessment of the

267 neoplastic and stromal compartments (**Fig. 4A**). Principle component analysis (PCA) and non-

268 supervised hierarchical clustering of the neoplastic transcriptomes clearly distinguished samples

269 from treatment naïve and alectinib-treated tumors at different treatment time points (**Fig. 4B, Fig**

270 **S6A**). Consistent with the lack of the baseline and early response differences between the NSG^{hHGF}

271 and NSG xenografts in tumor growth and spatial distributions of cell proliferation, transcriptional

272 analyses revealed the emergence of the HGF-dependent differences only after six weeks of

273 treatment (**Fig. 4B, Fig. S6A**). Pathway enrichment analyses indicated therapy-induced, HGF-

274 independent suppression of multiple pathways related to cell cycle, metabolism, and signaling, as

275 well as therapy-induced activation of PI3-AKT signaling, cellular senescence, and ECM-receptor

interactions (**Fig 4C**). To assess the utility of transcriptional inferences in identifying potential

therapeutic vulnerabilities, we assessed the impact of suppressing PI3K signaling, one of the

pathways differentially expressed between therapy-naïve and alectinib-treated tumors with PI3K

inhibitor alpelisib. Consistent with a recent report (28), alpelisib treatment significantly enhanced

tumor responses of xenograft tumors to alectinib, supporting the utility of the transcriptomics

inferences in identifying pathways mediating alectinib resistance (**Fig. S6B**).

PCA and hierarchical clustering analyses of transcriptional reads mapped to the mouse genome

revealed a clear impact of alectinib treatment on global transcriptomes. However, the effects of

the treatment duration and stromal expression of human HGF were less pronounced (**Fig. 4B, Fig.

S6A**). Pathway enrichment analyses revealed marked changes in multiple pathways involved in

ECM synthesis, degradation, and organization in alectinib-treated tumors (**Fig. 4C**). Consistent

with these changes, Mason Trichrome staining of histological samples revealed a therapy-induced

enhancement of collagen deposition (**Fig. S6C**). Additionally, IHC staining with hyaluronan-

binding protein revealed a substantial increase in the deposition of hyaluronan, which was

previously implied in microenvironmental therapy resistance (24) (29) (**Fig. S6D**).

The ECM-tumor cell interaction was dispensable for the ability of CAFs to reduce alectinib

sensitivity in our *in vitro* studies, as CM was capable of phenocopying the effects of CAF co-

cultures (**Fig. 1A**). However, we reasoned that this might be a reflection of specific experimental

conditions, as stronger resistance in physical CAF co-cultures was documented under higher cell

density and CAF/H3122 ratios (30). Integrin-mediated cell adhesion to collagens and fibronectin

is a well-established juxtacrine SMR mechanism documented in multiple contexts of targeted

therapies (31,32). Murine stroma expressed multiple ECM components implied in

microenvironmental resistance, while their expression was undetectable in human neoplastic cells

299   (**Fig. S6E**). To assess the potential contribution of collagens and fibronectin on the therapeutic

300   sensitivity of ALK+ NSCLC to ALKi, we contrasted the responses of H3122 and STE-1 cells

301   grown on regular tissue culture plastic with those grown on collagen-coated or fibronectin-coated

302   plates. We found that cells grown on the collagen and fibronectin matrix were substantially less

303   sensitive to both alectinib and crizotinib (**Fig. 4D, S7A**), supporting the potential involvement of

304   cell-ECM interactions in HGF-independent mediation of SMR to ALKi.

305   Next, we evaluated the potential involvement of paracrine-acting cytokines and growth factors

306   previously implied in microenvironment-mediated resistance to targeted therapies (8,12,13).

307   Transcriptional analyses revealed that similar to the genes encoding for ECM components,

308   expression of these growth factor genes was primarily confined to the stroma (**Fig. S6E**). While

309   not all the potential mediators exerted a detectable effect on alectinib sensitivity *in vitro*, multiple

310   EGF and FGF family growth factors as well as IGF1 and IL6, substantially reduced the sensitivity

311   of H3122 cells to alectinib in short-term growth assays and clonogenic studies (**Fig. 4E, Fig S7B,**

312   **C**), supporting their potential involvement in mediating the HGF-independent SMR effects *in vivo,*

313   where high local concentrations might be achieved in peristromal niches, compared to the dilutions

314   in the CAF CM. In summary, our analyses suggest that similar to the previously reported

315   multifactorial nature of cell-intrinsic therapy resistance (3,5), SMR might reflect an integrated

316   action of multiple juxtacrine and paracrine mechanisms.

317   **Targeting individual mechanisms is insufficient to overcome the effect of SMR.**

318   To assess the contribution of the HGF-independent SMR *in vivo*, we evaluated the impact of

319   pirfenidone on the alectinib sensitivity of H3122 tumors implanted in regular NSG mice.

320   Pirfenidone is a well-established anti-fibrotic agent that reduces fibroblast activation that acts by

321   suppressing the enhanced production of multiple ECM components and cytokines (33,34), thus

322   simultaneously suppressing multiple putative mechanisms that can mediate the HGF-independent

323   SMR. As expected, pirfenidone reduced the alectinib-induced increase in the deposition of

324   collagens in H3122 xenografts (**Fig. 5A**). While pirfenidone treatment did not impact tumor

325   growth, it substantially enhanced both the magnitude and the duration of alectinib-induced

326   remission (**Fig. 5B, S8A**). Given that the anti-fibrotic effects of pirfenidone are mediated by the

327   suppression of TGF-β production (33,34), we assessed the effects of an independent modulator of

328   TGFb responses using galunisertib, an inhibitor of TGF-β receptor I. Similar to pirfenidone,

329   galunisertib enhanced alectinib responses (**Fig. 5C, S8B**). Importantly, TGF-β has no direct effect

330   on reducing the sensitivity of H3122 cells to alectinib (**Fig. S7B**), enabling a straightforward

331   assessment of tumor cell-extrinsic effects. In summary, these results support the notion of a

332   substantial contribution of HGF-independent SMR mechanisms to *in vivo* therapeutic responses to

333   ALKi.

334   Next, we narrowed our analyses to assessing the contribution of more specific candidate

335   mechanisms of SMR. Hyaluronan, a common ECM component, is known to facilitate EM

336   resistance to EGFR/HER2 inhibitor lapatinib in breast cancers (24). Thus, we evaluated the effect

337   of the PEGylated recombinant human hyaluronidase (PEGPH20) (35), which substantially

338   reduced alectinib-induced hyaluronan deposition (**Fig. 5A**). Similar to pirfenidone, PEGPH20 co-

339   treatment substantially enhanced alectinib sensitivity of H3122 tumors (**Fig. 5B, S8A**). A similar

340   enhancement of alectinib sensitivity was observed with a co-inhibition of focal adhesion kinase

341   (FAK), which integrates juxtacrine effects of integrin-mediated adhesion to collagens and

342   fibronectins (**Fig. 5C, S8B**). To evaluate the relevance of HGF-independent paracrine

343   mechanisms, we assessed the contributions of FGF and EGF-mediated signaling by suppressing

344   their receptors. Consistent with our *in vitro* data (**Fig. 4E, S7C**), FGFR inhibitors erdafitinib and

345 infigratinib, and EGFR inhibitor gefitinib, enhanced alectinib sensitivity, delaying tumor

346 remissions (**Fig. 5C, D, S8B-D**). Notably, histological analyses of cell proliferation revealed that

347 none of the inhibitors of individual SMR mechanisms was able to suppress the proliferation of

348 tumor cells within peristromal niches completely (**Fig. S8E**), supporting the notion of the

349 multifactorial underpinning of the SMR (**Fig. 5E).**

350 **Targeting collateral sensitivities bypasses SMR.**

351 The combined contribution of multifactorial cell-intrinsic resistance and SMR to therapeutic

352 responses poses an obvious limitation to the success of the common strategy of identifying and

353 targeting a single persistence/resistance mechanism at a time. On the other hand, the feasibility of

354 simultaneous targeting of multiple mechanisms of cell-intrinsic and cell-extrinsic resistance is

355 limited by the iatrogenic challenge of additive toxicity. Potentially, this limitation can be addressed

356 by shifting therapeutic focus from targeting specific persistence/resistance mechanisms towards

357 targeting orthogonal collateral sensitivities of the residual tumors. Our previous work has revealed

358 that active transcriptional reprogramming during the acquisition of resistance to alectinib is

359 associated with the emergence of a strong collateral sensitivity to a dual EGFR/HER2 inhibitor

360 lapatinib, enabling to sidestep the challenge posed by multifactorial cell-intrinsic resistance (5).

361 Given the parallels between SMR and cell-intrinsic persistence, we assessed the impact of CAF

362 CM on lapatinib sensitivity. CAF1 CM exposure dramatically enhanced the lapatinib sensitivity

363 of H3122 and STE-1 cells in both short-term and clonogenic growth assays (**Fig. 6A, B** and **Fig.**

364 **S9A, B**). This effect was observed with CM from multiple fibroblast isolates (**Fig. S9C-E**) and,

365 unlike cell-intrinsic collateral sensitivity(5), was not dependent on alectinib pre-treatment.

366 Expression of both EGFR and HER2 protein was detectable in H3122 xenograft tumors at baseline

367 (**Fig. S9F, G**), and was further enhanced after two weeks of alectinib treatment, especially for

368   HER2 (**Fig. S9F**). Consistent with this observation and our previous report(5), lapatinib treatment

369   dramatically enhanced alectinib responses in H3122 xenografts, inducing stronger tumor

370   regression compared to the enhancement of individual SMR mechanisms (**Fig. 6C** and **Fig. S10A**).

371   However, the lapatinib-alectinib combination failed to eradicate H3122 tumors and suppress their

372   ability to develop resistance and relapse. Examination of relapsed tumors indicated that most of

373   the tumor cells have lost HER2 expression (**Fig. 6D** and **Fig. S10B**), suggesting a competitive

374   release of HER2-independent subpopulations or an acquired loss of HER2 dependence.

375   We reasoned that this therapeutic escape could be mitigated using a HER2-targeting antibody-drug

376   conjugate (ADC) trastuzumab-deruxtecan (T-DXd) in lieu of the small molecule inhibitor

377   lapatinib. Anti-tumor effects of trastuzumab do not rely on the cell's dependence on HER2

378   signaling, and the bystander effects of the T-DXd payload, topoisomerase inhibitor deruxtecan

379   enable targeting rare subpopulations that do not express HER2 (**Fig. 6E**). T-DXd strongly

380   enhanced the alectinib responses in H3122 xenograft tumors, driving 6/10 tumors below the

381   volumetric detectability threshold (**Fig. 6F** and **Fig. S10C**). Histological examination of the

382   injection sites revealed the presence of small pockets of residual disease composed of tumor cells

383   that lacked detectable HER2 expression (**Fig.S10D**). A strong enhancement of alectinib responses

384   was also observed in the STE-1 xenograft model. STE-1 xenograft tumors show stronger alectinib

385   sensitivity compared to H3122, and within six weeks of treatment, multiple tumors within both the

386   alectinib (4/10) and alectinib-T-DXd (8/10) treated groups regressed below volumetric

387   detectability threshold, complicating the comparison (**Fig. S10E**). To overcome this limitation, we

388   discontinued the treatment, focusing on the relapse dynamics. Whereas discontinuation of alectinib

389   treatment led to an immediate relapse, volumetrically detectable tumors post alectinib-T-DXd

390   treatment continued the regression, consistent with the lasting suppression of tumor cell growth

391 associated with cytotoxic chemotherapies (26). Eventually, all of the tumors became undetectable,

392 even after 11 weeks post discontinuation of treatment. Examination of the injection sites for

393 evidence of residual disease revealed that only two out of ten sites contained small pockets of

394 tumor cells. As with H3122 xenografts, residual STE-1 cells lost the detectable HER2 expression

395 (**Fig. S10F**). Notably, the small pockets of HER2- STE-1 cells were completely encapsulated by

396 hypertrophied fibrotic stromal tissue (**Fig. S10F**), suggesting a potential involvement of stromal

397 reaction in suppressing tumor growth relapse. Importantly, the switch to the alectinib-T-DXd

398 combination was able to restore therapeutic responsiveness in the tumors that have relapsed on

399 alectinib monotherapy, indicating its utility in reversing the acquired therapy resistance (**Fig.**

400 **S10G, H**). In summary, our results suggest that the challenge of the mechanistic complexity of

401 persistence and targeted therapies can be mitigated by shifting the focus from identifying and

402 targeting individual resistance-mediating pathways towards targeting collateral sensitivities and

403 using therapeutic agents with broader therapeutic effects.

404 **DISCUSSION**

405 Our study indicates that cancer's ability to avoid eradication by targeted therapies and to develop

406 resistance *in vivo* reflects a combined contribution of both cell-intrinsic resistance and SMR

407 mechanisms. SM effects dominate *in vivo* persistence (residual disease) while also contributing to

408 resistance (relapsed tumor growth). Importantly, our study indicates that, similar to the mechanistic

409 complexity of cell-intrinsic resistance (3,5), SMR represents a multifactorial, compound

410 phenotype that cannot necessarily be reducible to a single dominant mechanism. Together with a

411 generally recognized challenge of intra-tumor heterogeneity (2), this mechanistic complexity poses

412 an obvious challenge to the common therapeutic strategies of identifying and targeting a single

413 molecular mechanism. Our results suggest that this challenge can be partially mitigated by shifting

414 therapeutic focus towards exploiting collateral sensitivities of tumor cells within the residual

415 disease.

416 A large and growing body of experimental studies has demonstrated the ability of CAFs and other

417 non-neoplastic cell types within tumor stroma to reduce targeted therapy sensitivity in a wide range

418 of therapeutic contexts, particularly for targeted therapies (36). Mechanistically, these effects have

419 been attributed to multiple stroma-produced paracrine factors, including cytokines, ECM

420 components, metabolites, and non-coding RNAs within exosomes (36,37). Despite the multiplicity

421 of documented mechanisms, individual studies typically ascribe the SMR to a single dominant

422 mechanism per experimental system or tumor. Guided by the assumption of reducibility of CAF-

423 mediated resistance to a single mechanism, we identified HGF-cMET signaling as a pathway

424 predominantly responsible for CAF-mediated resistance *in vitro* (**Fig. 1**). However, our *in vivo*

425 studies revealed a more complex scenario, where the SMR involves the combined contribution of

426 several growth factors (HGF, FGF and EGF family ligands) and ECM components (integrins,

427 fibronectin and hyaluronic acid). Importantly, our study did not exhaust the assessment of all of

428 the potential SMR mechanisms uncovered in previous mechanistic studies, such as metabolic

429 crosstalk (37) and extracellular vehicle-mediated miRNA transfer(38). Therefore, SMR is likely

430 to be even more mechanistically complex, *e.g.*, including the contributions of additional molecular

431 mediators.

432 Notably, our results suggest that the relative contribution of different mechanisms might change

433 over the course of therapy. For example, whereas suppression of integrin signaling through a FAKi

434 defactinib and targeting hyaluronidase through PEGPH20 immediately enhanced alectinib

435 sensitivity (**Fig. 5B, C**), the effect of suppression of HGF-cMET and FGF-FGFR signaling could

436 only be detected after a significant delay (**Fig. 2C, E; Fig. 5C**). These differences might reflect

437 dynamic changes in both tumor and stromal microenvironment over the course of therapy, which

438 might not be reducible to a clean sequence of sensitivity-persistence-resistance, instead developing

439 over an eco-evolutionary resistance continuum, where the relative contribution of different

440 mechanisms changes over the course of the adaptation. Alternatively, the lack of detectable effects

441 of the HGF and FGF-mediated paracrine mechanisms during the earlier stages of response might

442 indicate that at the initial stages of adaptation, the survival and proliferation of tumor cells might

443 require a combined effect of both paracrine and juxtacrine mechanisms and thus can be only

444 detected within the immediate proximity to the stroma. Over the course of the treatment, carcinoma

445 cells within residual tumors develop partial cell-intrinsic resistance, which might enable them to

446 survive and proliferate beyond the immediate proximity to the stroma. However, the relatively

447 weak paracrine signals provide an additional fitness boost, enhancing tumor cell proliferation

448 beyond the immediate proximity to stroma, required for the juxtacrine signaling (Fig2H).

449 Given the spatial limitations of SMR action, knowledge of its molecular mechanisms is insufficient

450 for understanding its effects. The discrepancy between *in vitro* and *in vivo* findings highlights the

451 importance of spatial microenvironmental heterogeneity. Juxtacrine interactions with CAF-

452 produced ECM only impact tumor cells that are immediately adjacent to stroma, while multiple

453 cytokines capable of reducing therapy sensitivity to targeted therapies are likely to reach

454 sufficiently high concentrations only within the peristromal niche while being diluted in the CM.

455 Thus, adequate understanding of the SMR effects requires consideration of the characteristic

456 lengths scale of the paracrine action, stroma/tumor ratios, and spatial distribution of the protective

457 stroma niches. While the methodology to capture these effects has yet to be fully developed,

458 adequate quantitative inferences can be obtained through spatial analyses of histological images

459 and further adapting metrics from the fields of spatial statistics and spatial ecology (39-42) (**Fig.**

460 **3**). However, histological analyses only capture a single temporal snapshot. Given the temporal

461 dimension of the acquisition of therapy resistance uncovered in recent studies (5,10,43), an

462 adequate understanding of the impact of SMR calls for consideration of both spatial and also

463 temporal dynamics. This high complexity necessitates integrating mathematical modeling tools

464 like spatial agent-based models(44,45) or compartmentalized dynamical systems(44).

465 The contribution of SM mechanisms to in vivo therapy resistance and the mechanistic complexity

466 of SMR adds to the challenges posed by the diversity of resistance mechanisms, intratumor

467 heterogeneity(2) and the multifactorial nature of cell-intrinsic therapy resistance identified in

468 recent studies(5,10,43). While the development of new therapies relies on reductionistic molecular

469 oncology studies, the ability of tumor cells to resist therapeutic elimination and acquired therapy

470 resistance represents a complex dynamical phenomenon, integrating the impact of multiple cell-

471 intrinsic mechanisms, tumor heterogeneity, and systemic factors (such as inflammation(46) and

472 variability in drug concentrations due to pharmacokinetics modifiers(47)). Consequently, the

473 current paradigm of identifying and targeting a single mechanism at a time is unlikely to bring

474 major clinical breakthroughs. On the one hand, targeting individual mechanisms mediating SMR

475 or cell-intrinsic resistance can enhance the effect of the primary therapeutic agent (**Fig. 5B-D**). On

476 the other hand, co-targeting any resistance mechanism in isolation is insufficient to prevent the

477 ability of neoplastic populations to survive and adapt. At the same time, simultaneous co-targeting

478 of multiple resistance mechanisms is complicated by the issue of added toxicities and the moving

479 target nature of the tumors under treatment.

480 While our study examined a limited set of experimental models, the majority of well-studied

481 experimental models of targeted therapy responses are capable of persistence and evolved

482 resistance yet can also benefit from therapy-protecting interactions mediated by stroma-produced

483   ECM or growth factors. Of note, a complex interplay between cell-intrinsic resistance and SMR

484   has been recently reported for the development of therapy resistance in bone metastatic lesions of

485   multiple myeloma(48). Even though clinical analyses typically focus on cell-intrinsic resistance

486   mechanisms, a higher stroma/tumor ratio strongly correlates with poor therapy and survival

487   outcomes across multiple types of cancers, including NSCLC (49). This suggests the strong and

488   widespread contribution of SMR effects, a notion that is further supported by the observation of

489   therapy-induced spatial bias towards peristromal niches in clinical cancers (**Fig. 2G, Fig. S5**).

490   Our study highlights the potential utility of focusing on collateral vulnerabilities associated with

491   therapy persistence. At least in the H3122 and STE-1 experimental models, both adaptive

492   phenotypic rewiring during the acquisition of resistance to ALKi exposure to CAF produced

493   secreted factors lead to strong enhancement in sensitivity to the dual EGFR/HER2 inhibitor

494   lapatinib(5) (**Fig. 6B, Fig. S9A-E**). While we do not fully understand the underpinning of this

495   shared sensitivity, it might reflect a common denominator of partial EMT, associated with

496   enhanced phenotypic plasticity (37,50,51). Targeting this collateral sensitivity produces superior

497   responses compared to targeting individual molecular mediators of SMR (compare **Fig. 6C** with

498   **Fig. 5C, D**). However, the alectinib-lapatinib combination failed to eradicate the tumors and to

499   prevent them from adapting, likely reflecting the existence of HER2-independent therapeutic

500   escape mechanisms. This failure prompted us to consider the use of the antibody-drug conjugate

501   T-DXd which combines target specificity with an on-tumor bystander effect offered by antibody-

502   drug conjugates (**Fig. 6E**). While a subset of tumor cells still escaped eradication, the alectinib-T-

503   DXd combination induced very strong responses, and the residual tumors were unable to re-grow

504   after treatment discontinuation (**Fig. S10E**). Of note, a similar strong enhancement of tumor

505   responses to the primary targeted therapy by T-DXd was observed in a panel of models of

506 KRAS^{G12C} NSCLC (52), indicating a broad generalizability of our observations. In summary,

507 explicit consideration of the mechanistic complexity of resistance opens the door to the orthogonal

508 therapeutic strategies that mitigate this challenge.

509

510 **MATERIALS AND METHODS**

511

512 **Cell culture**

513 NSCLC cell lines H3122, STE-1, PC9, and H358 were obtained from the Lung Cancer Center of

514 Excellence Cell Line depository at Moffitt Cancer Center. HGF, GFP and mCherry-expressing

515 variants of H3122 cells were obtained as described(53). Cancer cell lines were cultured in RPMI

516 (Gibco, ThermoFisher) supplemented with 10% fetal bovine serum (FBS), 1%

517 penicillin/streptomycin, and 10μg/ml human recombinant insulin (Gibco) at 37°C and 5% CO_2.

518 All cell lines have been authenticated by short tandem repeat analysis.

519 Primary fibroblasts were derived from lung cancer patients' tumors or adjacent non-cancerous lung

520 tissue and were cultured in FB media as previously described(24). All human tissues were

521 collected using protocols approved by the H Lee Moffitt Cancer Center Institutional Review

522 Board. All cancer cell lines and fibroblast isolates were routinely tested for mycoplasma

523 contamination.

524 Fibroblast CM was generated by growing to ~ 80% confluency in FB media, at which point the

525 media was removed, the media was replaced with 10% FBS RPMI after a PBS wash. CM was

526 collected after 48 hours, filtered (0.2 μm), aliquoted, and either used immediately or stored at

527 −80°C. HGF concentration in the CM was determined using the human HGF ELISA Kit (Sigma-

528 Aldrich #RAB0212) following manufacturer protocol.

529   For collagen coating of tissue culture plates, rat tail collagen 1 was ordered from Thermo Fischer

530   (catalog #A1048301). Collagen 1 was further diluted to achieve 0.5 mg/ml in 0.02N glacial acetic

531   acid, plates were coated with the standard protocol as reported by the manufacturer. Plates were

532   then immediately used to seed cells for the experiment. Fibronectin-coated plates were ordered

533   from Stem Cell Technologies (catalog #100-1195).

534

535   ***In vitro* viability assays**

536   For short-term cell viability assay, 4000 cells per well were seeded in either RPMI or a 1:1 ratio

537   of RPMI: Fibroblast CM in a 96-well plate. Treatment was initiated the next day and lasted for 3

538   days. Cell viability was determined using CellTiterGlo reagent (Promega) following the

539   manufacturer's recommended protocol. The luminescence signal was determined using a GloMax

540   luminometer (Promega). For the analysis, the luminescence signal from the empty wells was

541   subtracted from each reading as the background, and % cell viability was determined relative to

542   DMSO-treated cells cultured in RPMI.

543   For cell viability in the co-culture setting, nuclear GFP labeled H3122 tumor cells were seeded

544   with unlabeled fibroblasts in a 1:1 ratio along with monoculture controls, to match the total number

545   of cells in the co-culture setting. The live cell images were acquired with the IncuCyte live cell

546   imaging system in the green fluoresce channel (software versions 2016A/B).

547   For low-density long-term colony formation assays, cells were seeded in either 6-well or 24-well

548   plates. Treatment was initiated 24 hours post seeding and lasted for 10 to 20 days. At the end point,

549   the cells were washed with cold 1X PBS and fixed with cold methanol. Tumor cell colonies were

550   stained with crystal violet solution (0.5% crystal violet solution in 25% methanol), followed by

551   water wash. Plates were allowed to dry overnight and then scanned to generate the images.

Reagents and cytokines

Alectinib, Crizotinib, Lorlatinib, Ceritinib, and Cabozantinib, were purchased from Fisher Scientific. Capmatinib, Sotorasib, and ARS-1620 were purchased from SelleckChem. Stock solutions of Brigatinib, Gefitinib, and Erlotinib were received as a kind gift from Uwe Rix lab at H Lee Moffitt Cancer Center. All drugs were dissolved in DMSO, aliquoted, and stored at −20°C. For the mouse studies, pharmaceutical grade alectinib, alpelisib, pirfenidone and T-DXd were received from the Lung Cancer Center of Excellence at Moffitt Cancer Center. Infigratinib, Galunisertib and Lapatinib was purchased from AstaTech. Capmatinib and Erdafitinib were purchased from MedChemExpress. Defactinib was purchased from Selleckchem.

The human HGF Antibody was purchased from R&D systems (AB-294-NA); murine HGF recombinant protein was purchased from Sino Biological (50038-MNAH-20). EGF (GMP100-15), HB-EGF (100-47), BTC (100-50), EREG (100-04), TGFα (100-16A), AREG (100-55B), BMP4 (GMP120-05ET), BMP6 (120-06), BMP7 (120-03P), TGFβ2 (100-35B), FGF1 (100-17A), FGF2 (100-18C), FGF7 (100-19), FGF10 (100-26), FGF9 (100-23), FGF18 (100-28), IL6 (200-06), IL11 (200-11), Activin A (120-14P) as well as murine growth factors & cytokines - IL11 (220-11), IL6 (216-16), FGF1 (450-33A), FGF2 (450-33), FGF7 (450-60), FGF10 (450-61), FGF9 (450-30), BTC (315-21), AREG (315-36), EGF (315-09) were purchased from PeproTech. Human recombinant NRG1 was purchased from BioLegend. We reconstituted these growth factors & cytokines in sterile 0.1% bovine serum albumin/ phosphate-buffered saline (FGF1- 5mM sodium phosphate and FGF2 - 5mM sodium chloride) and were stored at −20°C.

Animal studies

Xenograft studies were performed by subcutaneous bilateral implantation of 5E6 tumor cells/injection suspended 100 µl of 1: 1 RPMI / BME type 3 (R&D Systems #36-320-1002P). 4 to 6-week-old NOD-scid IL2Rgnull (NSG) or the NSG derivative NSG^{hHGF} (https://www.jax.org/strain/014553) recipient mice of both sexes. The animals were produced at the institute with breeders purchased from Jackson Laboratory. Treatment was initialized 3 weeks post implantation. Small molecule inhibitors were administered via daily oral gavages, 100 µl per dose. Alectinib and pirfenidone were dissolved in water. Capmatinib, Alpelisib, Erdafitinib, Defactinib, Galunisertinib and Lapatinib were suspended in MCT buffer (0.25% of methyl cellulose and 0.05% of Tween 80 in water). PEGPH20 was intravenously administered at 0.1 mg/kg twice a week. T-DXd was administered via intraperitoneal injections every 2 weeks.

Tumor diameters were recorded weekly using electronic calipers; tumor volumes were calculated assuming spherical-shaped tumors. 30-45 minutes prior to euthanasia, the animals were injected IP with 10 mg/ml BrdU dissolved in 1X PBS. The weights of excised tumors were recorded, and tumors were fixed in 10% formalin solution and/or snap-frozen (in liquid nitrogen) for further analyses. All the xenograft studies were performed per the approved procedures of IACUC protocol #IS00005557 of the H. Lee Moffitt Cancer Center. Animals were maintained under AAALAC-accredited specific pathogen-free housing vivarium and veterinary supervision following standard guidelines for temperature and humidity, with a 12-hour light/12-hour dark cycle.

Histological analyses

Formalin-fixed paraffin-embedded (FFPE) xenograft tumors were cut into 5-µm sections and mounted on glass slides. FFPE sections were deparaffinized and rehydrated, followed by heat-induced antigen retrieval in citrate buffer (pH 6.2). For immune histochemical staining, slides were incubated with 3% hydrogen peroxide in methanol followed by 10% goat serum blocking solution in 1X PBS for 10 min at room temperature. For BrdU staining, slides were incubated with primary anti-BrdU antibody (Roche,1117037600, 1:100) for 1 hour followed by the incubation with an anti-mouse biotinylated antibody (Vector Labs, BA-9200, 1:100) for 45 mins. For the detection of hyaluronic acid, slides were incubated with 4µg/ml biotinylated HABP (Sigma-Aldrich, catalog #385911) for 2.5 hours at room temperature. Detection of staining was performed with Vectastain ABC peroxidase reagent (Vector Laboratories, PK-6100) following the recommended protocol, using DAB as a colorimetric substrate and hematoxylin counterstain. Tissue collagen was detected using Masson Trichrome stain kit (Thermo Fisher, NC9752152) following manufacturer protocol. Following the staining, covering glass was mounted using permount^{TM} mounting media (Thermo Fisher, SP15-100). BrdU, HABP and Mason Trichrome stained sections were scanned with Aperio Scan Scope XT Slide Scanner (Leica).

For immunofluorescence staining, deparaffinized and rehydrated FFPE unstained tissue samples were heat incubated with antigen retrieval buffer (pH9 or pH6.2). Post one hour of incubation with blocking reagent (VectorLabs #S6000-100), tissues were incubated with primary antibodies against HER-2 (cell signaling, #4290T, 1:200) or EGFR (cell signaling, #4267, 1:50) and αSMA (Agilent, M085129, 1:100) overnight at +4C. Secondary antibody staining was performed using Alexa Fluor 488, goat anti-mouse IgG, (Invitrogen # A32723,1:1000), and Alexa Fluor 594, goat anti-rabbit IgG, (Invitrogen # A11012, 1:500) followed by nuclear staining with DAPI (Sigma-

621   Aldrich #D9542) (1:10,000 in PBS) for 10 mins at room temperature. Prior to cover slip mounting,

622   slides were treated with Vector Trueview autofluorescence quenching kit (VectorLabs, #SP-8400).

623   VECTASHIELD   (VectorLabs   #H-1200)   medium   was   used   for   slide   mounting.

624   Immunofluorescence   images   were   acquired   using   PhenoCycler-Fusion   system   (Akoya

625   Biosciences).

626

Tissue segmentation and spatial statistics analyses

628   Tissue segmentation was performed using the AI-assisted digital pathology platform Aiforia

629   version 5.2 as described in(54). Tissues were segmented into BrdU+/- tumor cells, stroma, and

630   necrotic tissue. The stromal areas identified by counterstaining were segmented as polygons

631   separating cellular and acellular-ECM components. Accuracy of tissue segmentation was vetted

632   by American Board of Pathology certified pathologist.

633   Spatial statistics analyses were performed using R 4.1.2. Point patterns were extracted from the

634   Aiforia-segmented histological images as described previously(54). Euclidian distance to the

635   nearest stroma pixel was determined for each of BrdU+ tumor cell. Cumulative density functions

636   of the distributions were used to perform comparison between BrdU+ and BrdU- tumor cells using

637   the Kolgomorov-Smirnoff (KS) test. To account for the variability in tumor/stroma distribution,

638   each sample was compared to an *in silico* random control, which retained spatial information on

639   each of the tumor cell and stromal pixel, but BrdU+ status was randomly redistributed among

640   tumor cells.

641

642

643

RNA-seq analyses

Snap-frozen xenograft tumor tissues were immersed in liquid nitrogen and physically disrupted with a mortar pestle. Total RNA was isolated using TRIzol reagent (Invitrogen, 15596026) according to the manufacturer's protocol. The concentration, quality, and integrity for total RNA was measured using NanoDrop and TapeStation system. cDNA library preparation and quality assessment were accomplished using Novogene's library guidelines. NovaSeq 6000 PE150 was used as a sequencing platform. Reads were mapped to the human - GRCh38 reference genome or murine - GRCm38/mm10 reference genome. Normalized reads were obtained from DeSeq2, and principal component analysis (PCA) was performed for Hg38 and mm10, to study transcriptomic changes in human tumor cells and murine stromal component of the tumor respectively.

To compare gene expression levels across baseline, remission, and relapse, we selected a list of significant genes per sample, using the DESeq2 R package(55). We filtered genes that have a fold change > |2| and false discovery rate (FDR) < 0.05. A ranked gene list was then created based on the genes' log2 fold change values. Next, we generated cluster maps for Hg38 and mm10 using these DEGs. The clusters so obtained on differential expression per sample indicate genes with similar expression patterns. After clustering, we calculated the z-scores for each row (each gene) and plot these instead of the log normalized expression values; this ensured the expression patterns that we want to visualize were highlighted and not confounded by the normalized expression values. Red color indicates genes with high expression levels, and blue color indicates genes with low expression levels. The cluster maps reinforce the presence of DEGs unique to each sample, and the potential effects of treatment on the DEGs.

Gene set enrichment analysis for the mouse and human mapped genes was performed, using the KEGG7 database(56) (www.kegg.jp) and RNAlysis software(57) to identify the biological

667   pathways that are significantly associated with each sample, and to assess the influence of

668   treatment. We considered KEGG terms with p-adj < 0.05 as significant enrichment. To visualize

669   the differential expressions of KEGG pathways across samples, we generated pathway heatmaps

670   using the NBBt-test R package(58).

671   **Statistical analyses**

672   In this study, all statistical analyses were performed using either Prism 9 (GraphPad Software) or

673   R statistical software (R Foundation for Statistical Computing). Details for the statistical tests are

674   provided in the figure legends. When relevant, the figure present experimental means ± SD or

675   mean ± SEM. P < 0.05 was considered as a significant.

676

677   **List of Supplementary Materials**

678   Fig. S1 to S8

679

References and Notes

1. Schneider JL, Lin JJ, Shaw AT. ALK-positive lung cancer: a moving target. Nat Cancer **2023**;4:330-43
2. Marusyk A, Janiszewska M, Polyak K. Intratumor Heterogeneity: The Rosetta Stone of Therapy Resistance. Cancer cell **2020**;37:471-84
3. Franca GS, Baron M, King BR, Bossowski JP, Bjornberg A, Pour M*, et al.* Cellular adaptation to cancer therapy along a resistance continuum. Nature **2024**
4. Vander Velde R, Shaffer S, Marusyk A. Integrating mutational and nonmutational mechanisms of acquired therapy resistance within the Darwinian paradigm. Trends Cancer **2022**
5. Vander Velde R, Yoon N, Marusyk V, Durmaz A, Dhawan A, Miroshnychenko D*, et al.* Resistance to targeted therapies as a multifactorial, gradual adaptation to inhibitor specific selective pressures. Nature Communications **2020**;11:2393
6. Meads MB, Gatenby RA, Dalton WS. Environment-mediated drug resistance: a major contributor to minimal residual disease. Nature reviews Cancer **2009**;9:665-74
7. Wilson TR, Fridlyand J, Yan Y, Penuel E, Burton L, Chan E*, et al.* Widespread potential for growth-factor-driven resistance to anticancer kinase inhibitors. Nature **2012**;487:505-9
8. Klemm F, Joyce JA. Microenvironmental regulation of therapeutic response in cancer. Trends Cell Biol **2015**;25:198-213
9. Hata AN, Niederst MJ, Archibald HL, Gomez-Caraballo M, Siddiqui FM, Mulvey HE*, et al.* Tumor cells can follow distinct evolutionary paths to become resistant to epidermal growth factor receptor inhibition. Nature medicine **2016**;22:262-9
10. Shaffer SM, Dunagin MC, Torborg SR, Torre EA, Emert B, Krepler C*, et al.* Rare cell variability and drug-induced reprogramming as a mode of cancer drug resistance. Nature **2017**;546:431-5
11. Ramirez M, Rajaram S, Steininger RJ, Osipchuk D, Roth MA, Morinishi LS*, et al.* Diverse drug-resistance mechanisms can emerge from drug-tolerant cancer persister cells. Nat Commun **2016**;7:10690
12. Sun Y. Tumor microenvironment and cancer therapy resistance. Cancer Lett **2016**;380:205-15
13. Bu L, Baba H, Yoshida N, Miyake K, Yasuda T, Uchihara T*, et al.* Biological heterogeneity and versatility of cancer-associated fibroblasts in the tumor microenvironment. Oncogene **2019**;38:4887-901
14. Wang W, Li Q, Yamada T, Matsumoto K, Matsumoto I, Oda M*, et al.* Crosstalk to stromal fibroblasts induces resistance of lung cancer to epidermal growth factor receptor tyrosine kinase inhibitors. Clinical cancer research : an official journal of the American Association for Cancer Research **2009**;15:6630-8
15. Yamada T, Takeuchi S, Nakade J, Kita K, Nakagawa T, Nanjo S*, et al.* Paracrine receptor activation by microenvironment triggers bypass survival signals and ALK inhibitor resistance in EML4-ALK lung cancer cells. Clinical cancer research : an official journal of the American Association for Cancer Research **2012**;18:3592-602
16. Hu H, Piotrowska Z, Hare PJ, Chen H, Mulvey HE, Mayfield A*, et al.* Three subtypes of lung cancer fibroblasts define distinct therapeutic paradigms. Cancer cell **2021**
17. Kaznatcheev A, Peacock J, Basanta D, Marusyk A, Scott JG. Fibroblasts and alectinib switch the evolutionary games played by non-small cell lung cancer. Nat Ecol Evol **2019**;3:450-6

18. Kogita A, Togashi Y, Hayashi H, Banno E, Terashima M, De Velasco MA, *et al.* Activated MET acts as a salvage signal after treatment with alectinib, a selective ALK inhibitor, in ALK-positive non-small cell lung cancer. Int J Oncol **2015**;46:1025-30

19. Remsing Rix LL, Sumi NJ, Hu Q, Desai B, Bryant AT, Li X, *et al.* IGF-binding proteins secreted by cancer-associated fibroblasts induce context-dependent drug sensitization of lung cancer cells. Sci Signal **2022**;15:eabj5879

20. Sharma SV, Lee DY, Li B, Quinlan MP, Takahashi F, Maheswaran S, *et al.* A chromatin-mediated reversible drug-tolerant state in cancer cell subpopulations. Cell **2010**;141:69-80

21. Lavie D, Ben-Shmuel A, Erez N, Scherz-Shouval R. Cancer-associated fibroblasts in the single-cell era. Nat Cancer **2022**;3:793-807

22. Matsumoto K, Nakamura T. Hepatocyte growth factor and the Met system as a mediator of tumor-stromal interactions. Int J Cancer **2006**;119:477-83

23. Jeffers M, Rong S, Vande Woude GF. Hepatocyte growth factor/scatter factor-Met signaling in tumorigenicity and invasion/metastasis. J Mol Med (Berl) **1996**;74:505-13

24. Marusyk A, Tabassum DP, Janiszewska M, Place AE, Trinh A, Rozhok AI, *et al.* Spatial Proximity to Fibroblasts Impacts Molecular Features and Therapeutic Sensitivity of Breast Cancer Cells Influencing Clinical Outcomes. Cancer research **2016**;76:6495-506

25. Srivastava AK, Navas T, Herrick WG, Hollingshead MG, Bottaro DP, Doroshow JH, *et al.* Effective implementation of novel MET pharmacodynamic assays in translational studies. Ann Transl Med **2017**;5:3

26. Miroshnychenko D, Miti T, Kumar P, Miller A, Laurie M, Giraldo N, *et al.* Stroma-mediated breast cancer cell proliferation indirectly drives chemoresistance by accelerating tumor recovery between chemotherapy cycles. Cancer research **2023**

27. Gardner A, de Mingo Pulido A, Hanggi K, Bazargan S, Onimus A, Kasprzak A, *et al.* TIM-3 blockade enhances IL-12-dependent antitumor immunity by promoting CD8(+) T cell and XCR1(+) dendritic cell spatial co-localization. J Immunother Cancer **2022**;10

28. Talwelkar SS, Mayranpaa MI, Schuler J, Linnavirta N, Hemmes A, Adinolfi S, *et al.* PI3Kbeta inhibition enhances ALK-inhibitor sensitivity in ALK-rearranged lung cancer. Mol Oncol **2023**;17:747-64

29. Toole BP, Slomiany MG. Hyaluronan: a constitutive regulator of chemoresistance and malignancy in cancer cells. Semin Cancer Biol **2008**;18:244-50

30. Hu Q, Remsing Rix LL, Desai B, Miroshnychenko D, Li X, Welsh EA, *et al.* Cancer-associated fibroblasts confer ALK inhibitor resistance in EML4-ALK -driven lung cancer via concurrent integrin and MET signaling. bioRxiv **2024**

31. Hirata E, Girotti MR, Viros A, Hooper S, Spencer-Dene B, Matsuda M, *et al.* Intravital imaging reveals how BRAF inhibition generates drug-tolerant microenvironments with high integrin beta1/FAK signaling. Cancer cell **2015**;27:574-88

32. Cooper J, Giancotti FG. Integrin Signaling in Cancer: Mechanotransduction, Stemness, Epithelial Plasticity, and Therapeutic Resistance. Cancer cell **2019**;35:347-67

33. Ruwanpura SM, Thomas BJ, Bardin PG. Pirfenidone: Molecular Mechanisms and Potential Clinical Applications in Lung Disease. Am J Respir Cell Mol Biol **2020**;62:413-22

34. Schaefer CJ, Ruhrmund DW, Pan L, Seiwert SD, Kossen K. Antifibrotic activities of pirfenidone in animal models. Eur Respir Rev **2011**;20:85-97

35. Wong KM, Horton KJ, Coveler AL, Hingorani SR, Harris WP. Targeting the Tumor Stroma: the Biology and Clinical Development of Pegylated Recombinant Human Hyaluronidase (PEGPH20). Curr Oncol Rep **2017**;19:47

36. Sahai E, Astsaturov I, Cukierman E, DeNardo DG, Egeblad M, Evans RM, *et al.* A framework for advancing our understanding of cancer-associated fibroblasts. Nature reviews Cancer **2020**;20:174-86

37. Fiori ME, Di Franco S, Villanova L, Bianca P, Stassi G, De Maria R. Cancer-associated fibroblasts as abettors of tumor progression at the crossroads of EMT and therapy resistance. Mol Cancer **2019**;18:70

38. Yang F, Ning Z, Ma L, Liu W, Shao C, Shu Y*, et al.* Exosomal miRNAs and miRNA dysregulation in cancer-associated fibroblasts. Mol Cancer **2017**;16:148

39. Clark PJ, Evans FC. Distance to Nearest Neighbor as a Measure of Spatial Relationships in Populations. Ecology **1954**;35:445-53

40. van Lieshout MNM, Baddeley AJ. A nonparametric measure of spatial interaction in point patterns. Statistica Neerlandica **1996**;50:344-61

41. Szmyt J. Spatial statistics in ecological analysis: from indices to functions. Silva Fennica **2014**;48

42. Miti T, Desai B, Miroshnychenko D, Basanta D, Marusyk A. Dissecting the Spatially Restricted Effects of Microenvironment-Mediated Resistance on Targeted Therapy Responses. Cancers **2024**;16:2405

43. França GS, Baron M, King BR, Bossowski JP, Bjornberg A, Pour M*, et al.* Cellular adaptation to cancer therapy occurs by progressive state transitions along a resistance continuum. Nature **2024**;In Press

44. Altrock PM, Liu LL, Michor F. The mathematics of cancer: integrating quantitative models. Nature reviews Cancer **2015**;15:730-45

45. Quaranta V, Weaver AM, Cummings PT, Anderson AR. Mathematical modeling of cancer: the future of prognosis and treatment. Clin Chim Acta **2005**;357:173-9

46. Greten FR, Grivennikov SI. Inflammation and Cancer: Triggers, Mechanisms, and Consequences. Immunity **2019**;51:27-41

47. Meertens M, Muntinghe-Wagenaar MB, Sikkema BJ, Lopez-Yurda M, Retel VP, Paats MS*, et al.* Therapeutic drug monitoring guided dosing versus standard dosing of alectinib in advanced ALK positive non-small cell lung cancer patients: Study protocol for an international, multicenter phase IV randomized controlled trial (ADAPT ALEC). Front Oncol **2023**;13:1136221

48. Bishop RT, Miller AK, Froid M, Nerlakanti N, Li T, Frieling JS*, et al.* The bone ecosystem facilitates multiple myeloma relapse and the evolution of heterogeneous drug resistant disease. Nat Commun **2024**;15:2458

49. Zhang T, Xu J, Shen H, Dong W, Ni Y, Du J. Tumor-stroma ratio is an independent predictor for survival in NSCLC. Int J Clin Exp Pathol **2015**;8:11348-55

50. Shibue T, Weinberg RA. EMT, CSCs, and drug resistance: the mechanistic link and clinical implications. Nat Rev Clin Oncol **2017**;14:611-29

51. Singh A, Settleman J. EMT, cancer stem cells and drug resistance: an emerging axis of evil in the war on cancer. Oncogene **2010**;29:4741-51

52. Ozakinci H, Desai B, Kalos D, Chen D-T, Henry M, Solanki H*, et al.* Trastuzumab Deruxtecan Combination Strongly Enhances Responses and Overcomes Sotorasib Resistance in KRAS^{G12C}-Mutant NSCLC. bioRxiv **2024**:2024.12.17.628751

53. Marusyk A, Tabassum DP, Altrock PM, Almendro V, Michor F, Polyak K. Non-cell-autonomous driving of tumour growth supports sub-clonal heterogeneity. Nature **2014**;514:54-8

54. Giugliano F, Corti C, Tarantino P, Michelini F, Curigliano G. Bystander effect of antibody-drug conjugates: fact or fiction? Curr Oncol Rep **2022**;24:809-17

55. Love MI, Huber W, Anders S. Moderated estimation of fold change and dispersion for RNA-seq data with DESeq2. Genome Biol **2014**;15:550

56. Kanehisa M, Goto S. KEGG: kyoto encyclopedia of genes and genomes. Nucleic Acids Res **2000**;28:27-30

827 57. Teichman G, Cohen D, Ganon O, Dunsky N, Shani S, Gingold H, *et al.* RNAlysis: analyze
828   your RNA sequencing data without writing a single line of code. BMC Biol **2023**;21:74
829 58. Tan YD, Guda C. NBBt-test: a versatile method for differential analysis of multiple types of
830   RNA-seq data. Sci Rep **2022**;12:12833

831

846 **Author contributions:** BD and AM conceptualized the study and co-wrote the manuscript. BD,

847   TM, DM, MH, and VM were responsible for the methodology. BD was responsible for

848   the majority of experimental studies, analyses and visualizations. MH and AM performed

849   animal experiments. VM performed IHC and IF staining. DM has developed tissue

850   segmentation pipeline; BD, DM and CG performed histological image analyses. TM,

851   DB, AM and PA developed spatial statistics pipeline; TM performed the spatial analyses.

852   MB provided advice on image segmentation and vetted the segmentation accuracy. BD

853   and TM performed statistical analyses. AM supervised the project. Funding was acquired

854   by AM, DB, JS, EH and AA. All authors contributed to the review of the manuscript.

855   **Competing interests:** The authors declare no competing interests.

856   **Data and materials availability:** All data are available in the main text or the supplementary

857   materials.

858
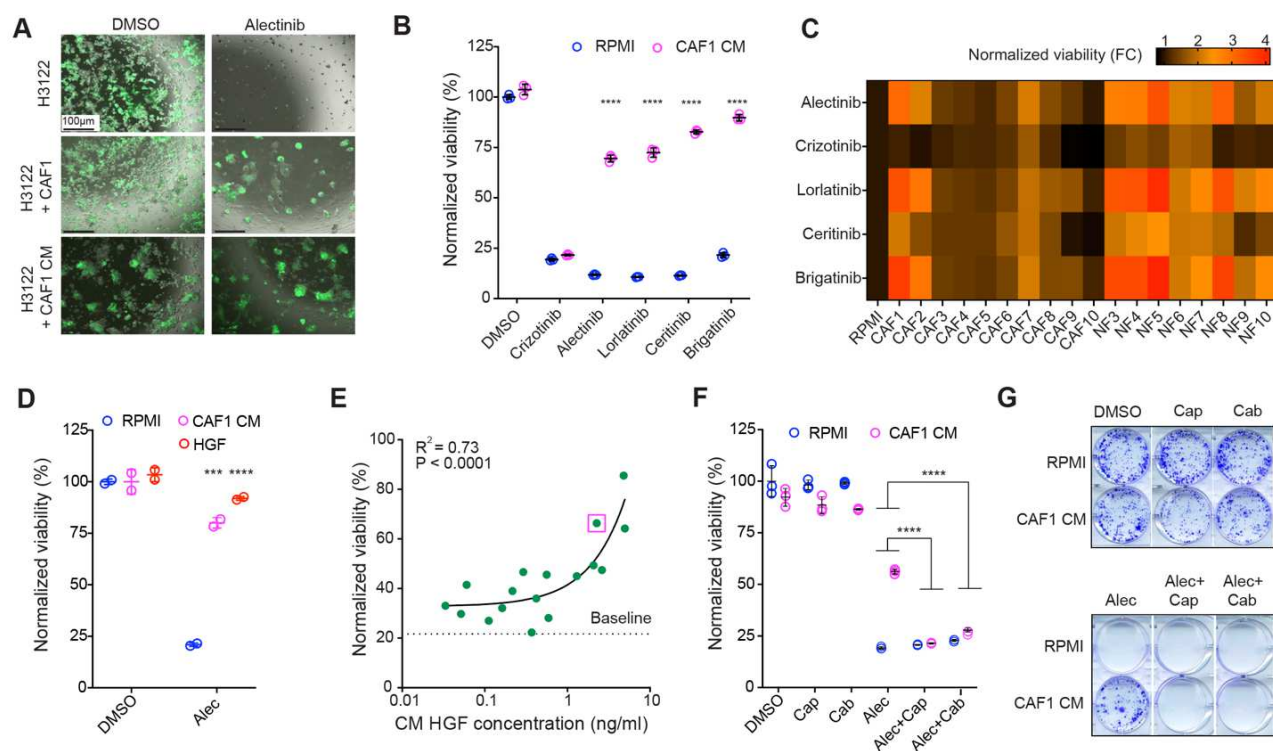
Fig. 1. Fibroblasts protect ALK+ NSCLC from ALKi through the HGF-cMET axis. (**A**) Live fluorescent microscopy images of GFP labeled H3122 cells co-cultured with unlabeled CAFs or CAF1 CM in the presence of alectinib (0.5μM) or DMSO vehicle control. (**B**) Cell Titer-Glo viability assay of H3122 cells cultured in RPMI or CAF CM with DMSO control, crizotinib (0.5 μM), alectinib (0.25 μM), lorlatinib (0.5 μM), ceritinib (0.1 μM) and brigatinib (0.25 μM). Results are normalized to the DMSO control signal in RPMI. (**C**) Heatmap summary of the impact of fibroblast CM on sensitivity to H3122 cells to the indicated ALKi. The sensitivity is presented as the fold change in cell viability as compared to the RMPI media control**. (D**) Exogenous HGF at the concentration found in CAF1 CM (2 ng/ml) phenocopies alectinib-protecting effect of CAF1 CM. (**E**) Pearson correlation analysis of the correlation between HGF levels detected in the CM of individual fibroblast isolates and the impact of CM on alectinib (0.1 μM) sensitivity. Purple square highlights CAF1 CM. (**F, G**) cMET inhibitors capmatinib (0.2 μM) and cabozantinib (0.2 μM) overcome protective effect of CAF1 CM to alectinib (0.25 μM) in short-term (4d) viability assay (F) and longer-term clonogenic survival assay (**10d**), (**G**). *** and **** indicate $p<0.001$ and $p<0.0001$, respectively, of the interaction term of two-way ANOVA assay, comparing the impact of CM on viability of H3122 cells under treatment with ALKi versus vehicle control (DMSO) (B, D), or on viability of H3122 cells under alectinib in the absence or presence of cMET inhibitors (F).
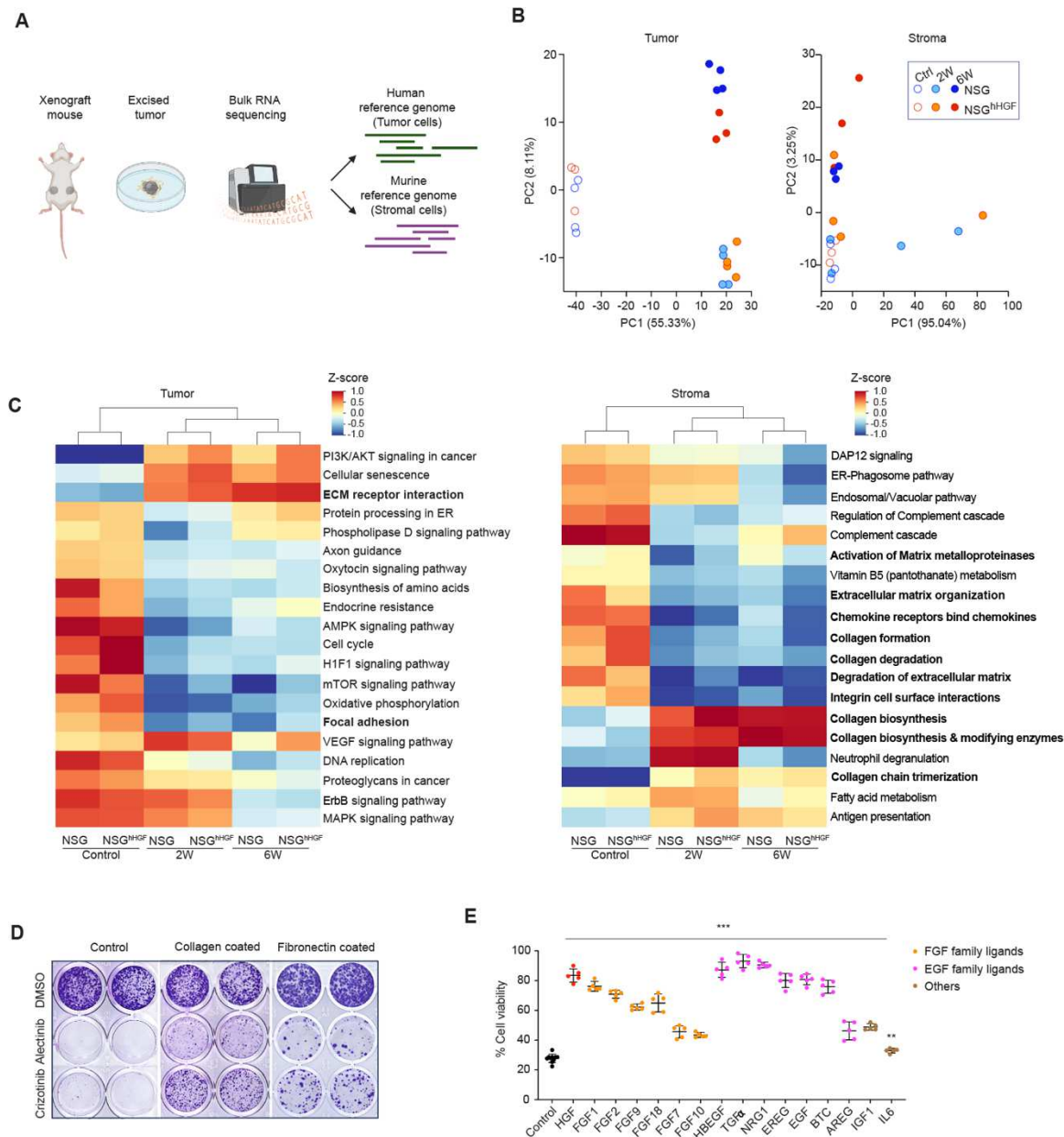
Figure 2
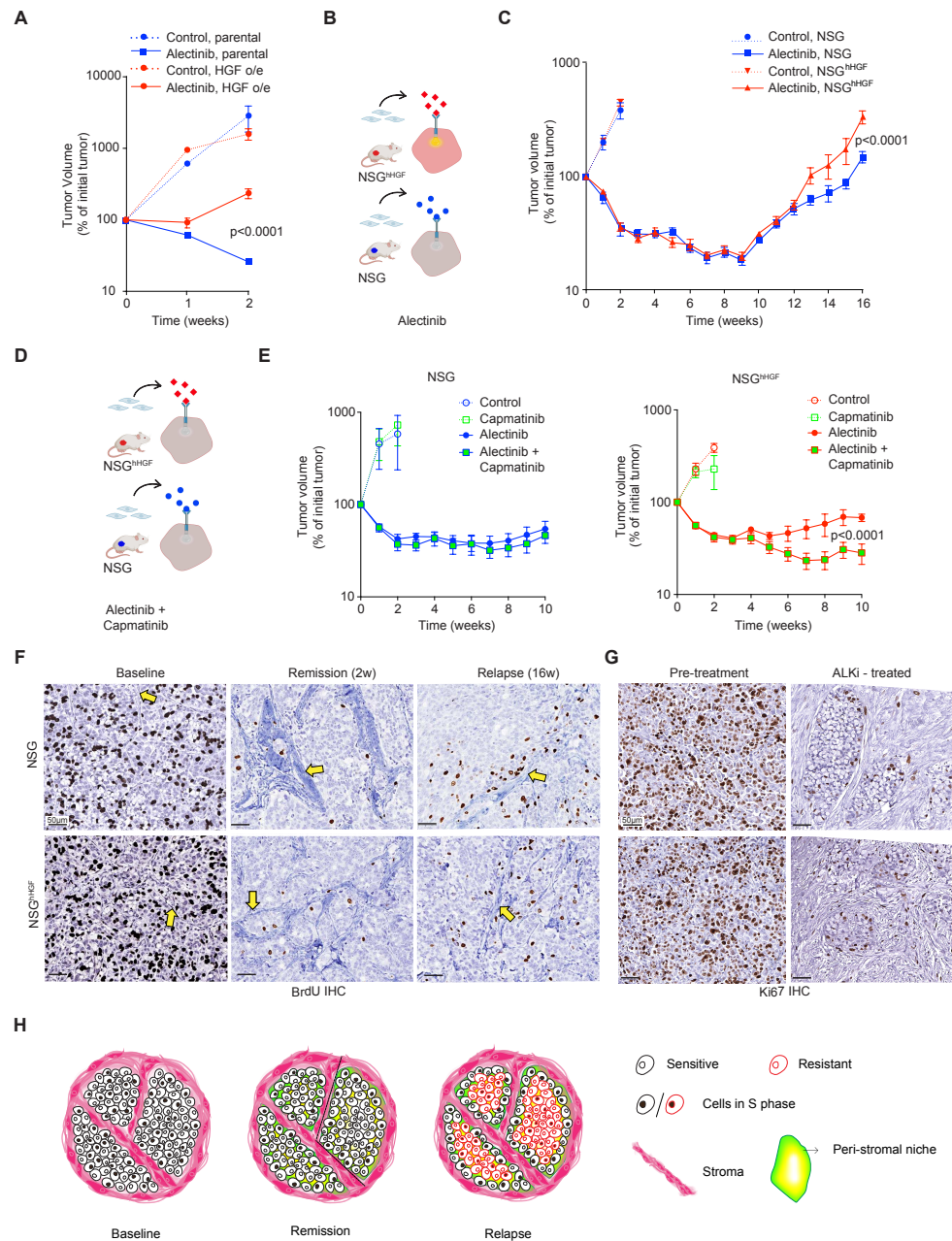
Fig. 2. Stromal mediated resistance effects involve HGF independent mechanisms *in vivo*. (A) Exogenous expression of HGF confers resistance to alectinib (25 mg/kg) in NSG xenografts. N=4 tumors for all groups except for HGF o/e control (N=2). Error bars represent SEM. **(B)** Diagram of the experimental design to assess the impact of stromal activation of tumor cMET -mediated bypass signaling *in vivo*. **(C)** Volumetric response dynamics of H3122 xenograft tumors in NSG and NSG^hHGF hosts, continuously treated with 25 mg/kg alectinib or vehicle control. Error bars represent SEM; N= 4 & 18 for the control and alectinib-treated groups, respectively. **(D)** Diagram of the experimental idea: cMET inhibition should suppress the enhanced relapse in NSG^hHGF xenografts. **(E)** Tumor response dynamics for vehicle control (N=4), 40 mg/kg capmatinib (N=4), 20 mg/kg alectinib (N=10) and alectinib/capmatinib (N=10) combination treated groups respectively. **(F)** Representative images of anti-BrdU IHC from xenograft tumor tissues at the indicated time points. Arrows point to the examples of stromal regions defined by counterstain. P values in tumor growth analyses represents the significance of the interaction term of the repeated measurement 2-way ANOVA analyses between the indicated groups. **(G)** Representative images of anti-KI67 IHC tumor tissue from pre-treatment or post ALKi treatment of patient diagnosed with ALK+ NSCLC. H. Conceptual model for the contribution of SMR to the *in vivo* therapeutic responses
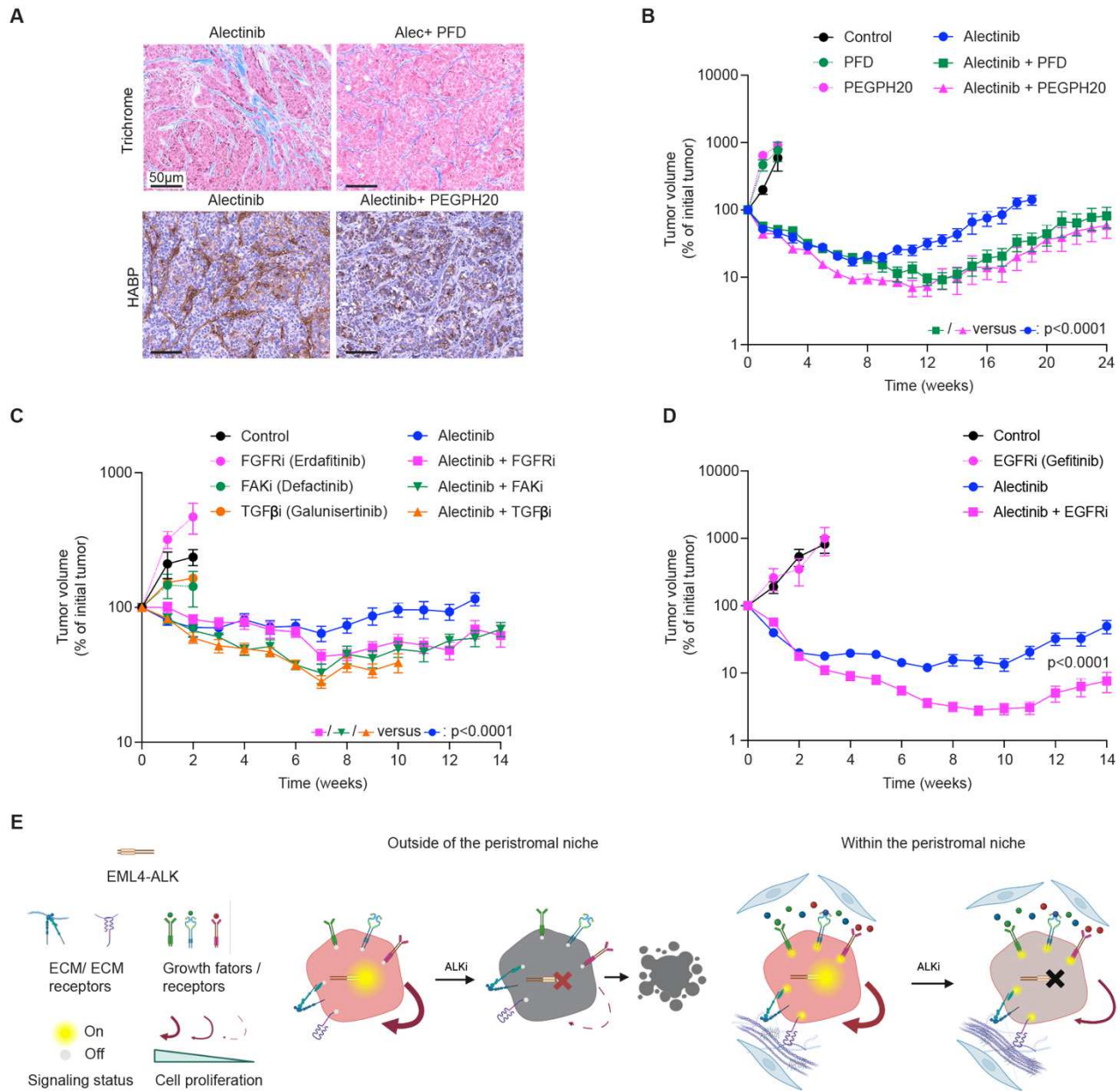
Figure 3
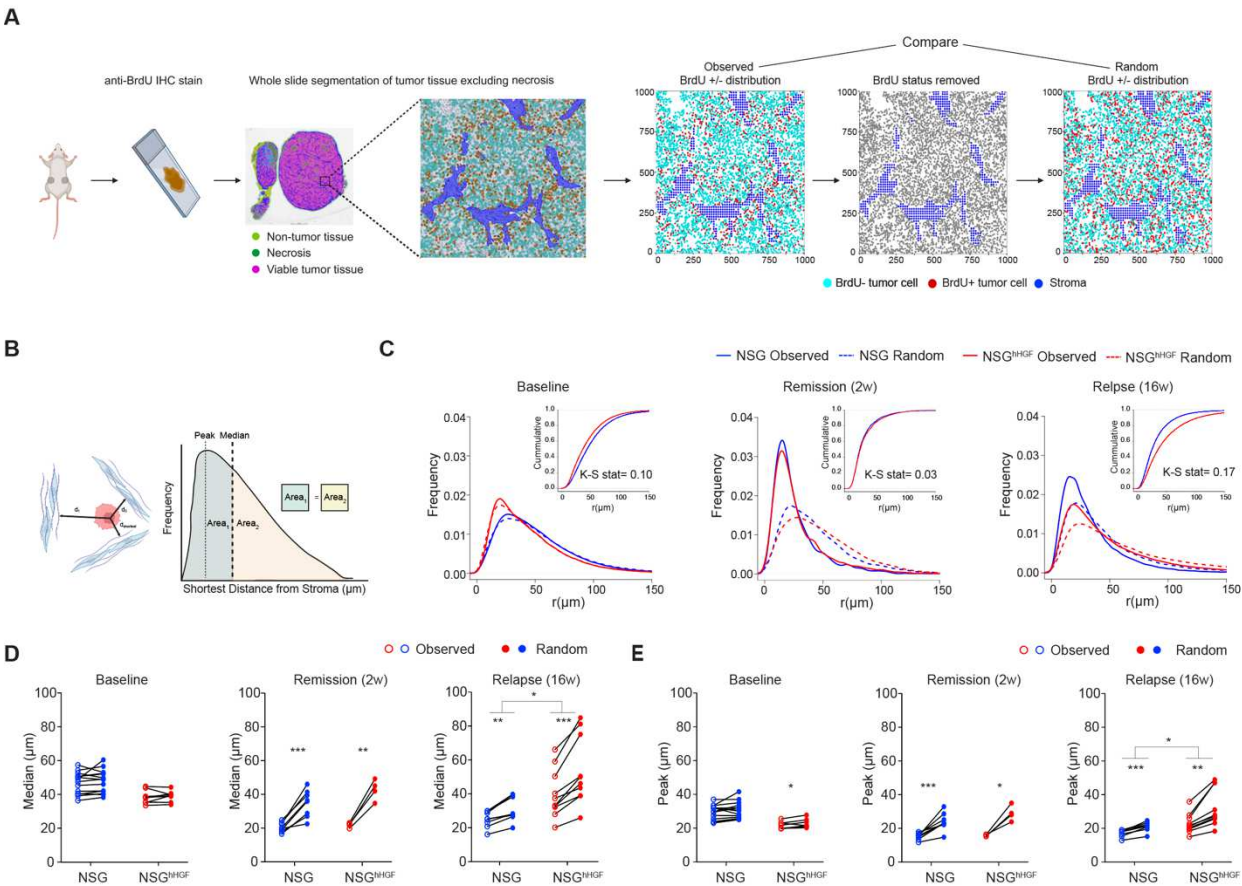
Fig. 3. Spatial analyses of tumor tissues indicate HGF-independent sheltering from cytostatic effects of alectinib in peristromal niches. (**A**) Diagram of the spatial analysis workflow. (**B**) Diagram depicting analyses of distances to the nearest stroma. (**C**) Observed and random distributions of the distances of BrdU+ cells to the nearest stroma; cumulative distribution and KS statistics values are shown as insets. (**D, E**) Ladder plots comparing the medians (D) and means (E) of predicted and observed distributions of the distances of BrdU+ cells to the nearest stroma. Each point reflects an analysis of a whole cross-section of an individual tumor. *, **, *** indicate p values of less than 0.05, 0.01, and 0.001, respectively. Comparisons between the observed and predicted values were performed using a 2-tailed t-test; comparisons between NSG and NSG^{hHGF} models were performed with the analyses of the interaction term of 2-way ANOVA test. KS denotes Kolmogorov-Smirnov test.
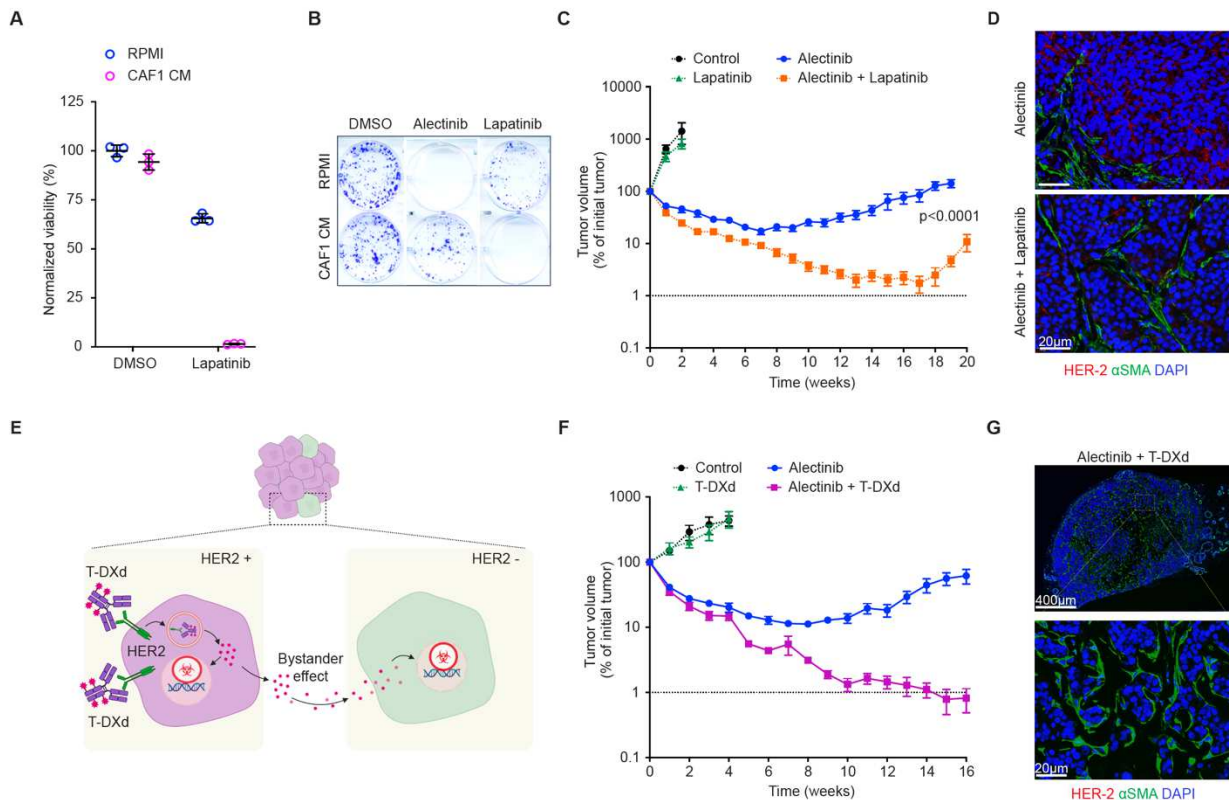
Figure 4

Figure 4. Transcriptomic analyses of tumor and stromal components identify the potential HGF-independent mechanisms of stroma-mediated therapy resistance. (A) Diagram for transcriptional analyses approach. (**B**) PCA analyses of neoplastic and stromal transcriptomes. (**C**) Non-supervised hierarchical clustering of pathway analyses of differentially expressed genes. Bolded font indicates pathways related to ECM production and remodeling. (**D**) Crystal violet stain of clonogenic assay of H3122 cells seeded into control, collagen or fibronectin coated plates cultured for 20 days in 0.1 μM alectinib, 0.5 μM crizotinib or DMSO control. (**E**) Cell Titer Glo viability assay for H3122 cells cultured in 0.1 μM alectinib in the presence of indicated growth factors (50ng/ml). ** and *** indicate $p<0.01$ and $p<0.001$ respectively for the 2-tailed Mann Whitney test comparing alectinib sensitivity between the control samples and samples treated with the indicated growth factors
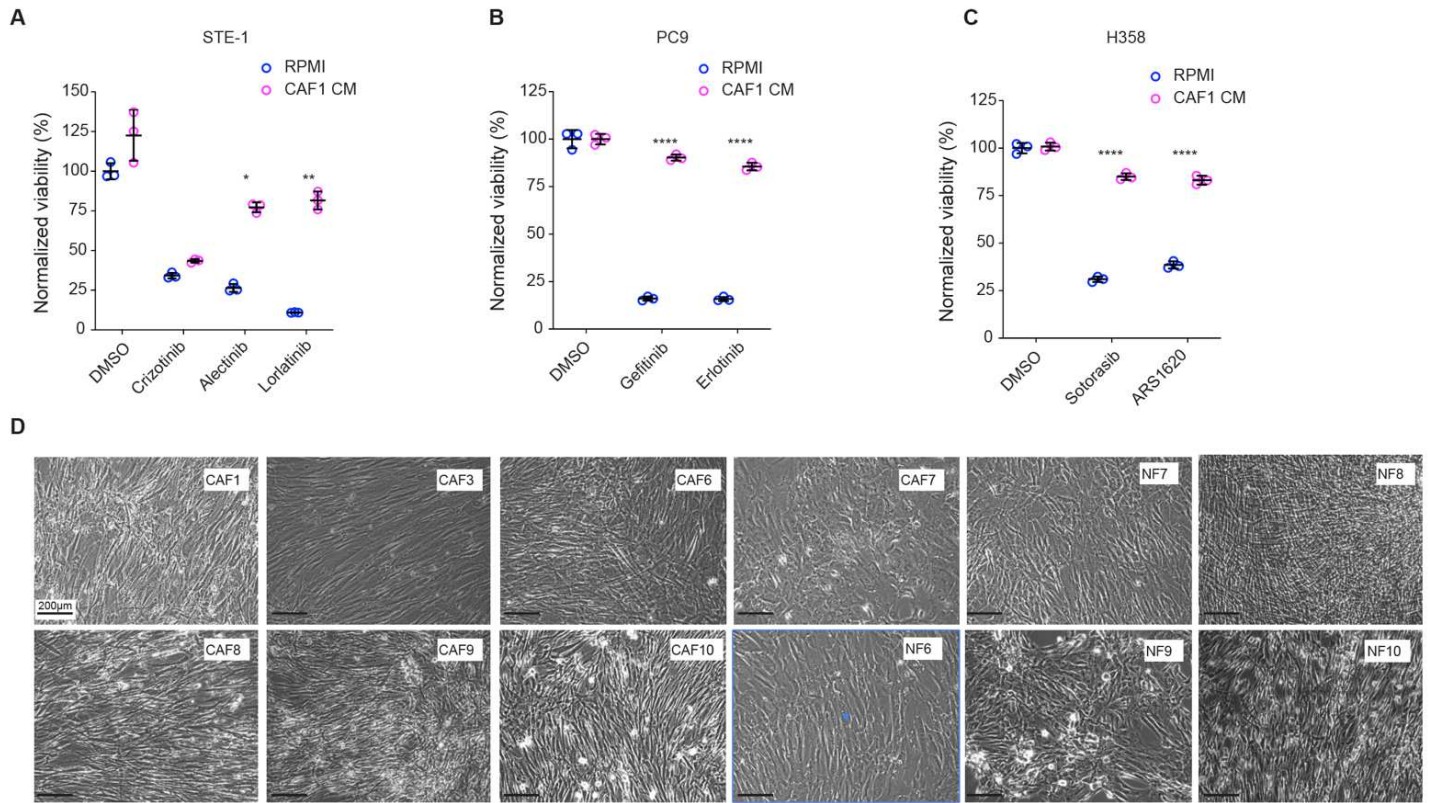
Figure 5

Figure 5. Suppression of multiple candidate mechanisms of stromal resistance improves responses to ALKi. (**A**) Pirfenidone and PEGPH20 treatment suppresses alectinib-induced enhancement of collagen (Mason Trichrome staining, upper panel) and hyaluronan (lower panel) deposition, respectively. (**B**) Volumetric responses of H3122 xenograft tumors to vehicle (N=4), 900 mg/kg pirfenidone (N=6), 0.1 mg/kg PEGPH20 (N=6), 25 mg/kg alectinib (N=10), alectinib/PEGPH20 and alectinib/pirfenidone combinations (N=10). (**C**) Volumetric responses of H3122 xenograft tumors to vehicle, 20 mg/kg erdafitinib, 50 mg/kg defactinib, 75 mg/kg galunisertib, 20 mg/kg alectinib and the indicated combinations. N=6 for the control and individual co-inhibitors. N=10 for the alectinib and the combination treatment groups. (**D**) Volumetric responses of H3122 xenograft tumors to vehicle, 20 mg/kg alectinib, 40 mg/kg gefitinib and alectinib/gefitinib combination. N=10 for the alectinib and combination treatment groups, N=6 for the control and gefitinib group. P values indicate the result of the interaction group of repeated measurement ANOVA comparing combination therapies to the alectinib monotherapy. (**E**) Diagram of the conceptual model. Peristromal niche location enables tumor cells to partially maintain viability and proliferation upon ALK inhibition due to multiple ECM and growth factor signaling mechanisms. Outside of the peristromal niche, cells lack the compensating mechanisms, leading to a more complete proliferation arrest and apoptosis.

Figure 6

Figure 6. Targeting collateral sensitivity associated with stromal proximity overcomes the limitations of multifactorial resistance. (**A**) Impact of CAF1 CM on sensitivity of H3122 cells to 10 µM lapatinib in 4 days CellTiter-Glo assay. (**B**) Impact of CAF1 CM on sensitivity of H3122 cells to 0.1 µM alectinib and 10 µM lapatinib in 10 days Crystal Violet clonogenic assay. (**C**) Response dynamics of H3122 xenograft tumors treated with vehicle control (N=5), 100 mg/kg lapatinib (N=6), 25 mg/kg alectinib (N=10) and alectinib/lapatinib combination (N=10). Error bars represent SEM. (**D**) Representative images of IF staining against HER-2 (red) and αSMA (green) of xenograft tumors from (C) at the experimental endpoint. (**E**) Diagram of the experimental idea: targeting of HER2 expressing cells with the antibody-drug conjugate T-DXd should lead to elimination of the rare HER2- cells via bystander effect. (**F**) Response dynamics of H3122 xenograft tumors treated with vehicle control (N=4), 10 mg/kg T-DXd (N=8), 25 mg/kg alectinib (N=8) and alectinib/T-DXd combination (N=10). (**G**) Representative images of whole tumor against HER-2 (red) and αSMA (green) of xenograft tumors collected at the endpoint of the experiment shown in (F).

Figure S1
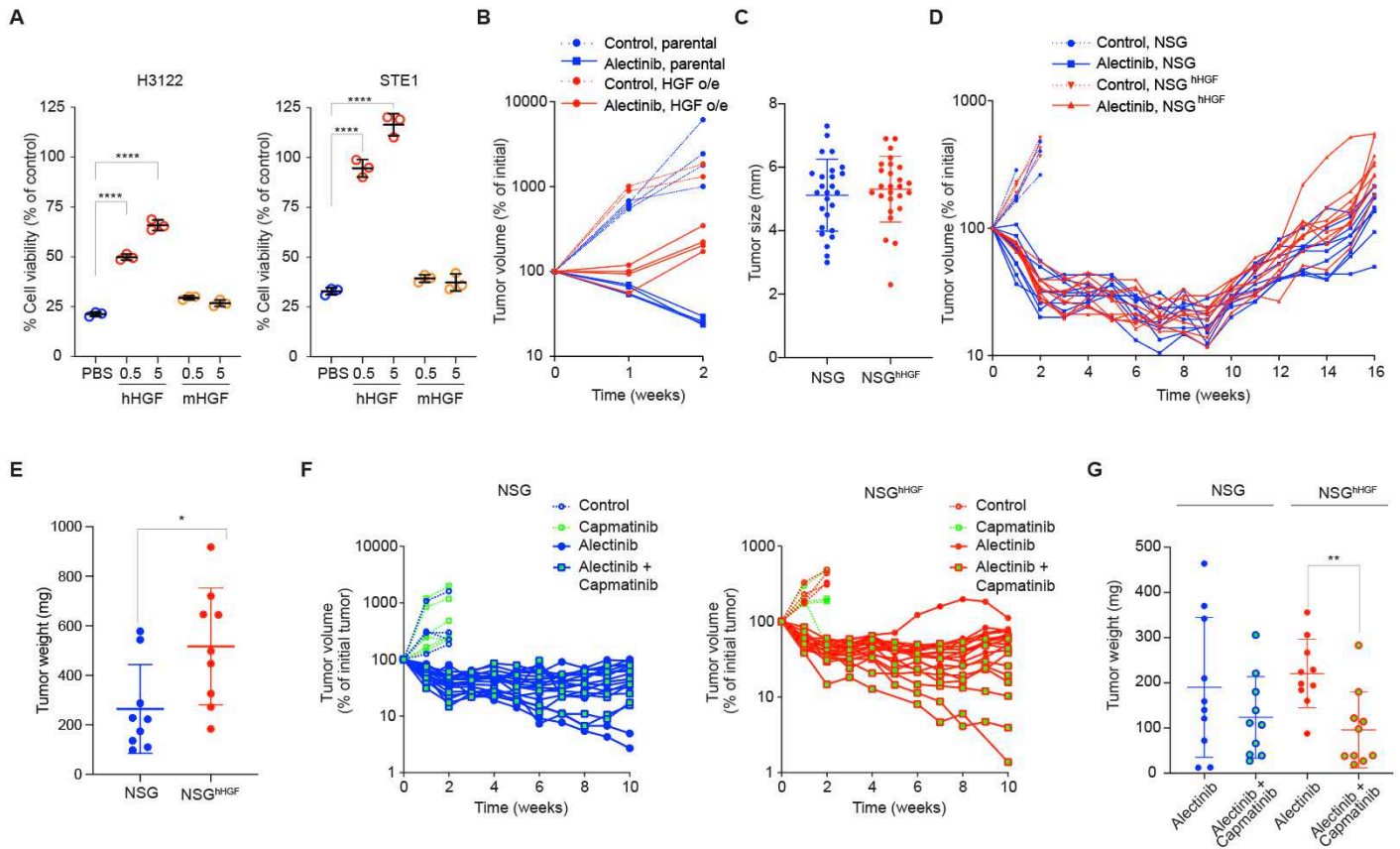

Figure S1. (**A)** Impact of CAF CM on the viability of STE1 cells in crizotinib (0.5 µM), alectinib (0.25 µM), lorlatinib (0.5 µM) and DMSO control. (**B**) Impact of CAF CM on the viability of PC9 cells in gefitinib (0.25 µM), erlotinib (0.25 µM) and DMSO control (**C**) Impact of CAF CM on the viability of H358 cells in sotorasib (0.05 µM), ARS1620 (1 µM) and DMSO control. *, **and **** refers to p<0.05, p<0.01 and p<0.0001, respectively, of the interaction term of two-way ANOVA assay, comparing the impact of CM on viability between DMSO and treatment groups. (**D**) Representative microscopy images of cultures of normal and cancer-associated fibroblasts, 10x magnification.

Figure S2
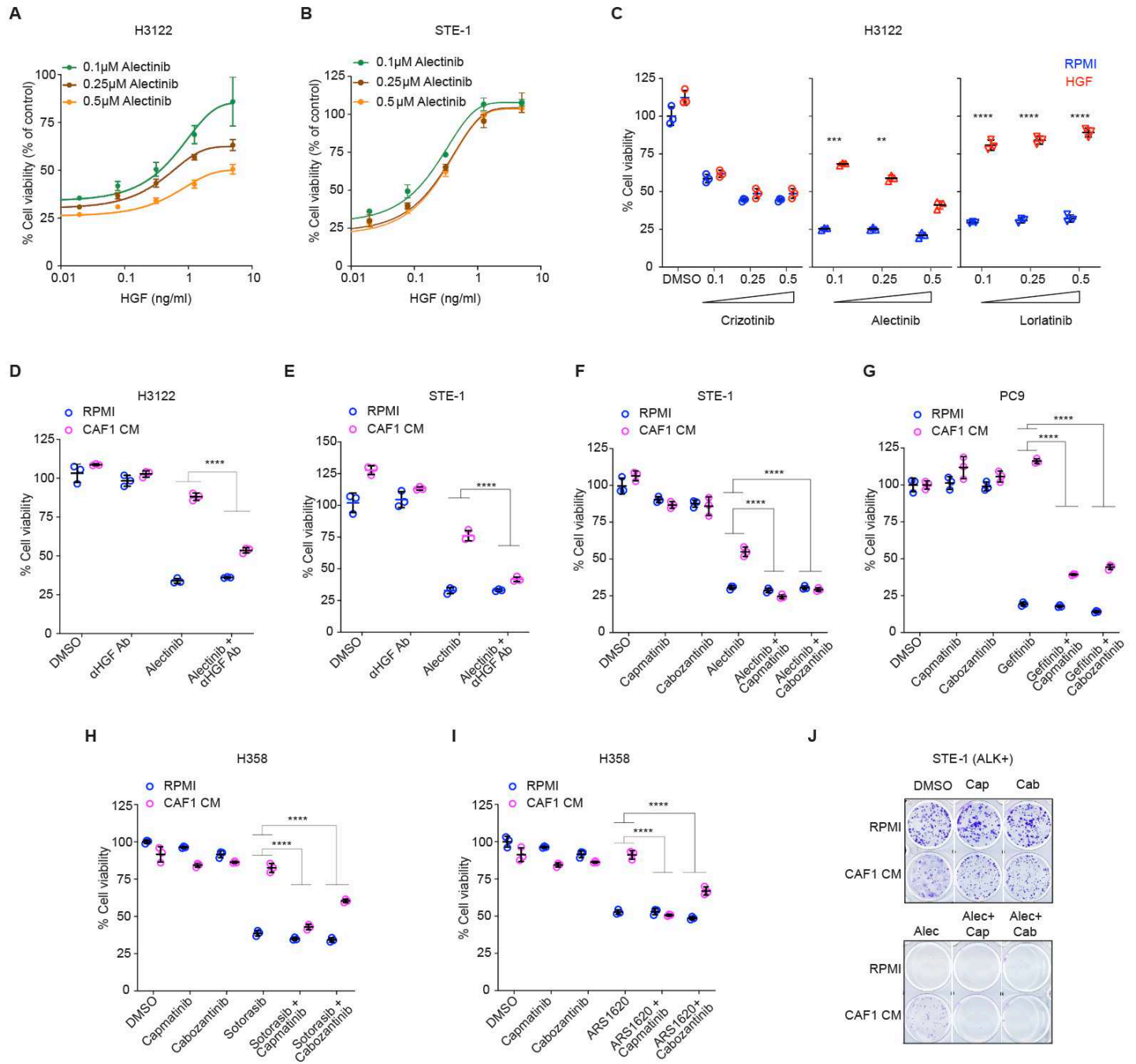
Figure S2. Effect of the indicated concentrations of HGF on the viability of H3122 (**A**) and STE1 (**B**) cells under the indicated alectinib concentrations. (**C**) Impact of HGF (2 ng/ml) on the viability of H3122 cells under the indicated concentrations of ALKi. (**D**, **E**) Impact of HGF neutralizing antibody (2.5 µg/ml) on the viability of H3122 (D) and STE1 (E) cells in 0.1 µM of alectinib. (**F-I**). Impact of cMET inhibitors cabozantinib (0.2 µM) and capmatinib (0.2 µM) on the sensitivity of STE-1 cells to 0.1 µM alectinib (F), PC9 cells to 0.25 µM gefitinib (G), H358 cells to 0.05 µM sotorasib (H) and 1 µM ARS1620 (I). **, ***, and **** indicate $p<0.01$, $p<0.001$, and $p<0.0001$ of the interaction term of 2-way ANOVA between the indicated groups. J. Microscopy images of the crystal violet stain of the 10-day culture of STE1 cells under 0.2 µM capmatinib, 0.2 µM cabozantinib, 0.1 µM alectinib, cMETi/alectinib combinations and DMSO control.

Figure S3. (**A**) Impact of the indicated concentrations of human and murine HGF on the viability of H3122 and STE1 cells under 0.1 µM alectinib. (**B**). Volumetric traces of individual parental and HGF expressing H3122 xenograft tumors treated with 25 mg/kg alectinib or vehicle control. (**C**) Tumor sizes (diameters) of xenograft tumors in NSG and NSGhHGF hosts pre-treatment. Each dot represents an individual tumor. (**D**) Volumetric traces of individual H3122 xenograft tumors in NSG and NSGhHGF hosts treated with 25 mg/kg alectinib or vehicle control. (**E**) Final tumor weights from the experiment depicted in (D). (**F**). Volumetric data of individual H3122 xenograft tumors treated with 40mg/kg capmatinib, 25 mg/kg alectinib or vehicle control in NSG (left panel) or NSGhHGF (right panel) hosts. (**G**). Final tumor weights from the experiment depicted in (F).
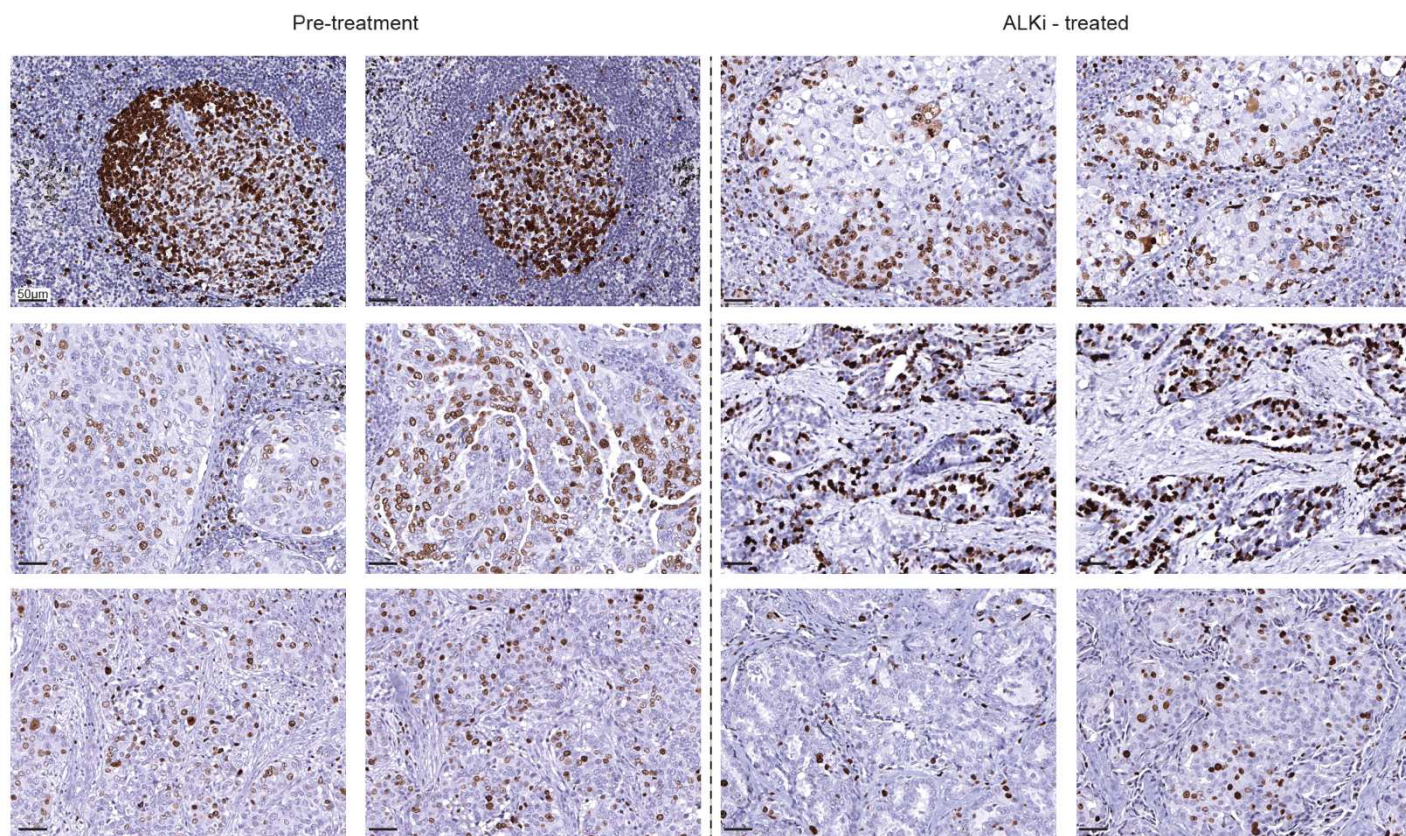
Figure S4
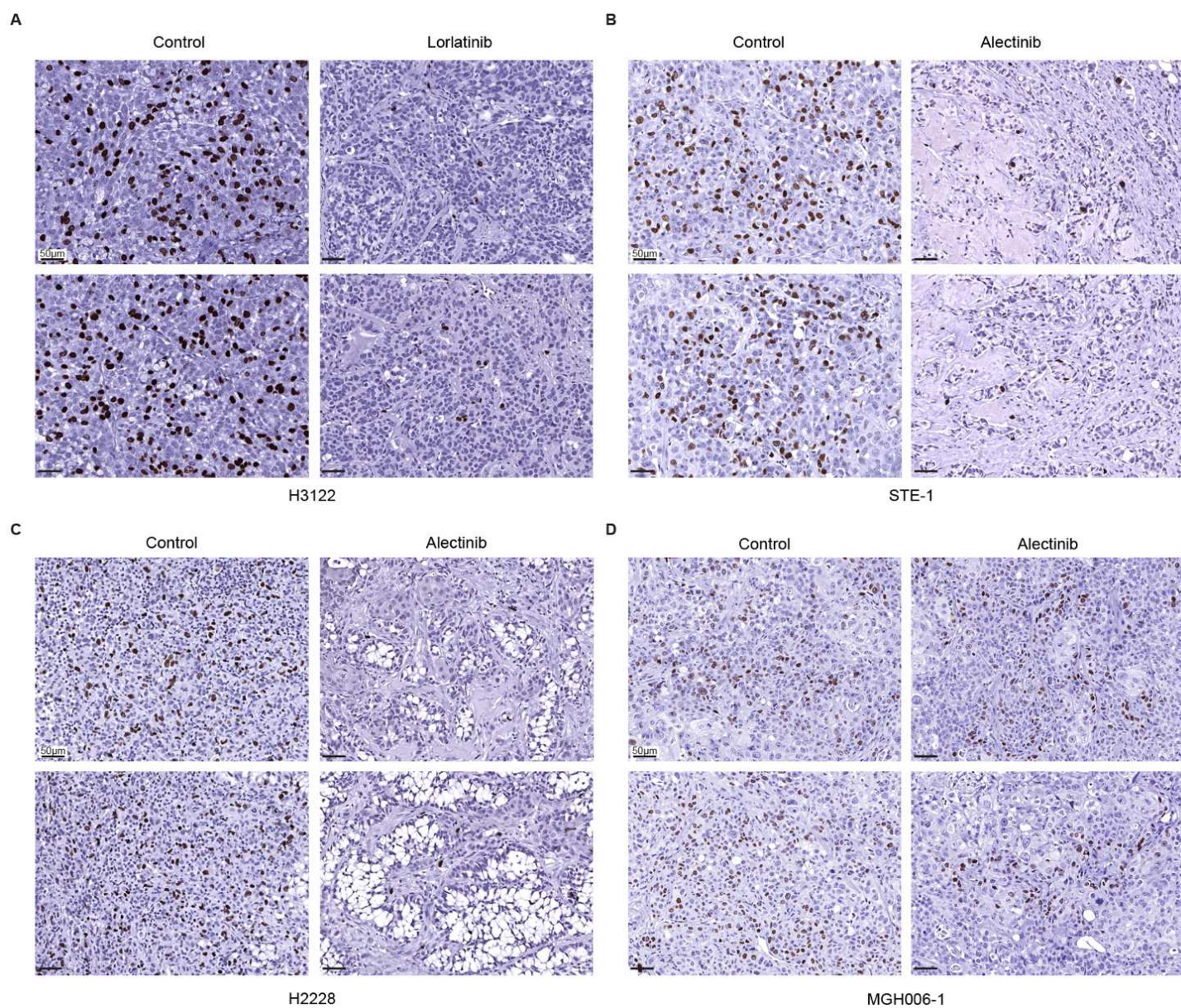
Figure S4. Representative images of anti-BrdU IHC staining of tumors tissues from H3122 (**A**), STE-1 (**B**), H2228 (**C**) and MGH006-1 (**D**) xenograft mice treated with the indicated therapies.

Figure S5

Pre-treatment   ALKi - treated

Figure S5. Representative images of anti-KI67 IHC tumor tissue from pre-treatment (left panel) or post ALKi treatment (right panel) of patient diagnosed with ALK+ NSCLC.
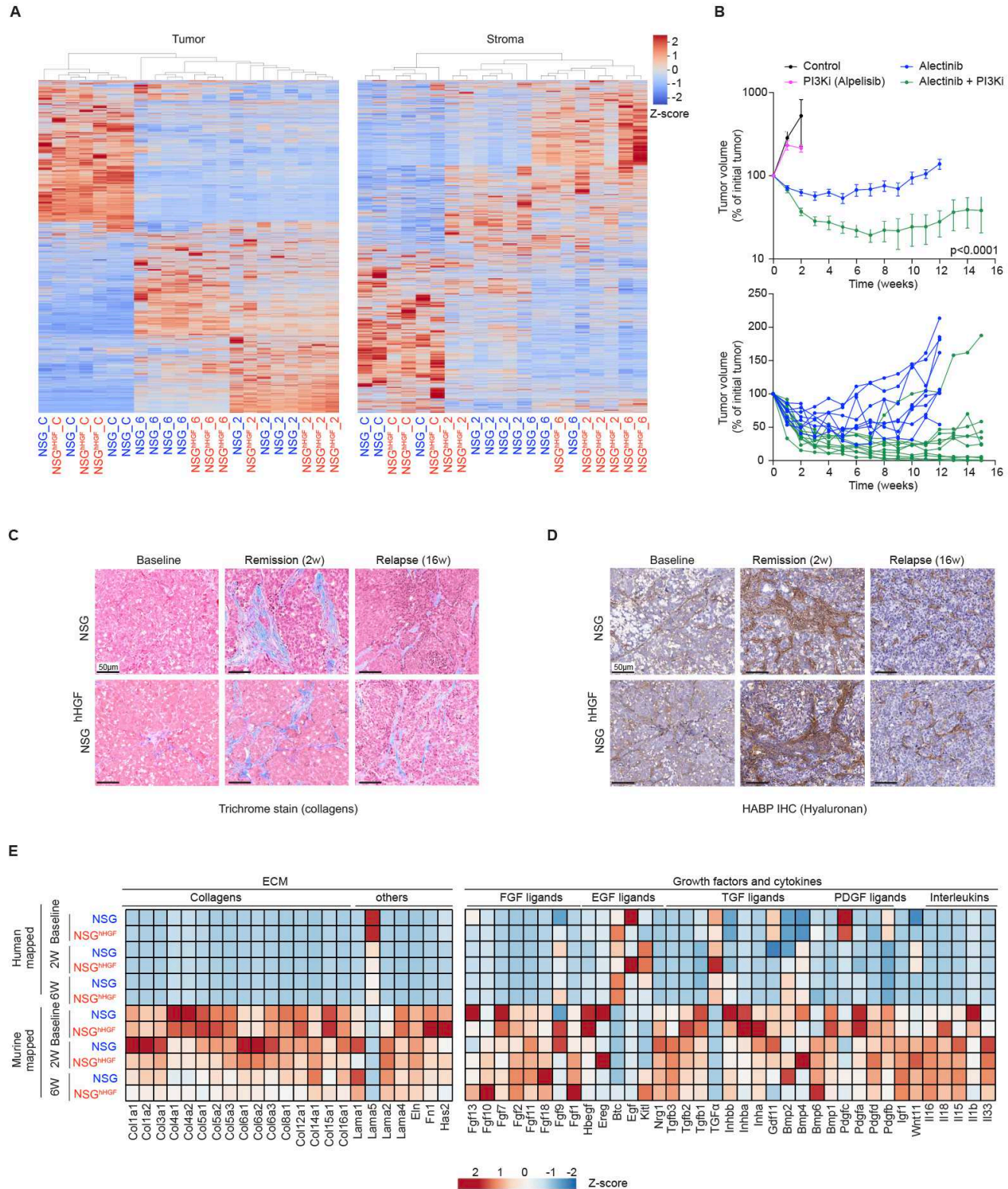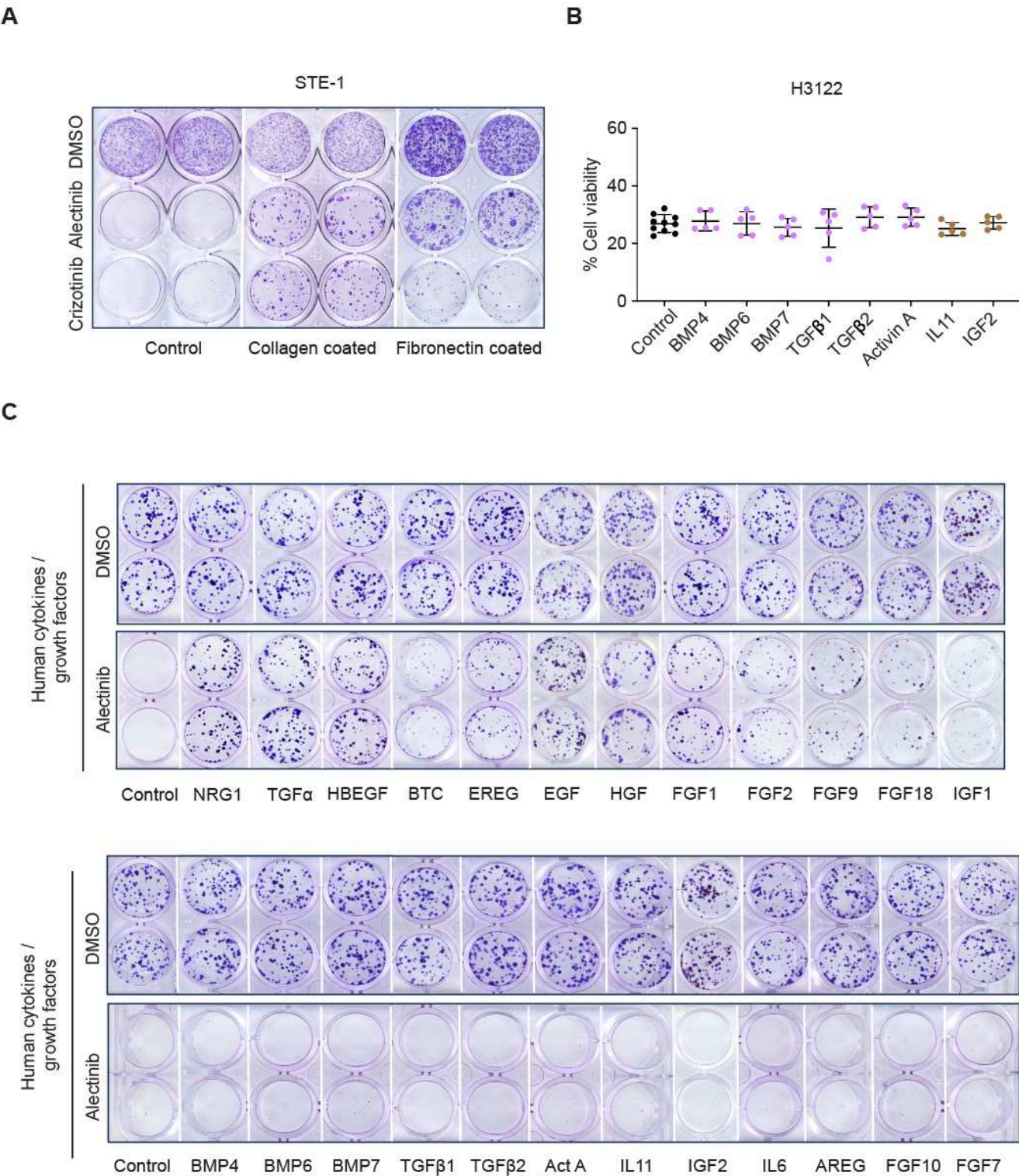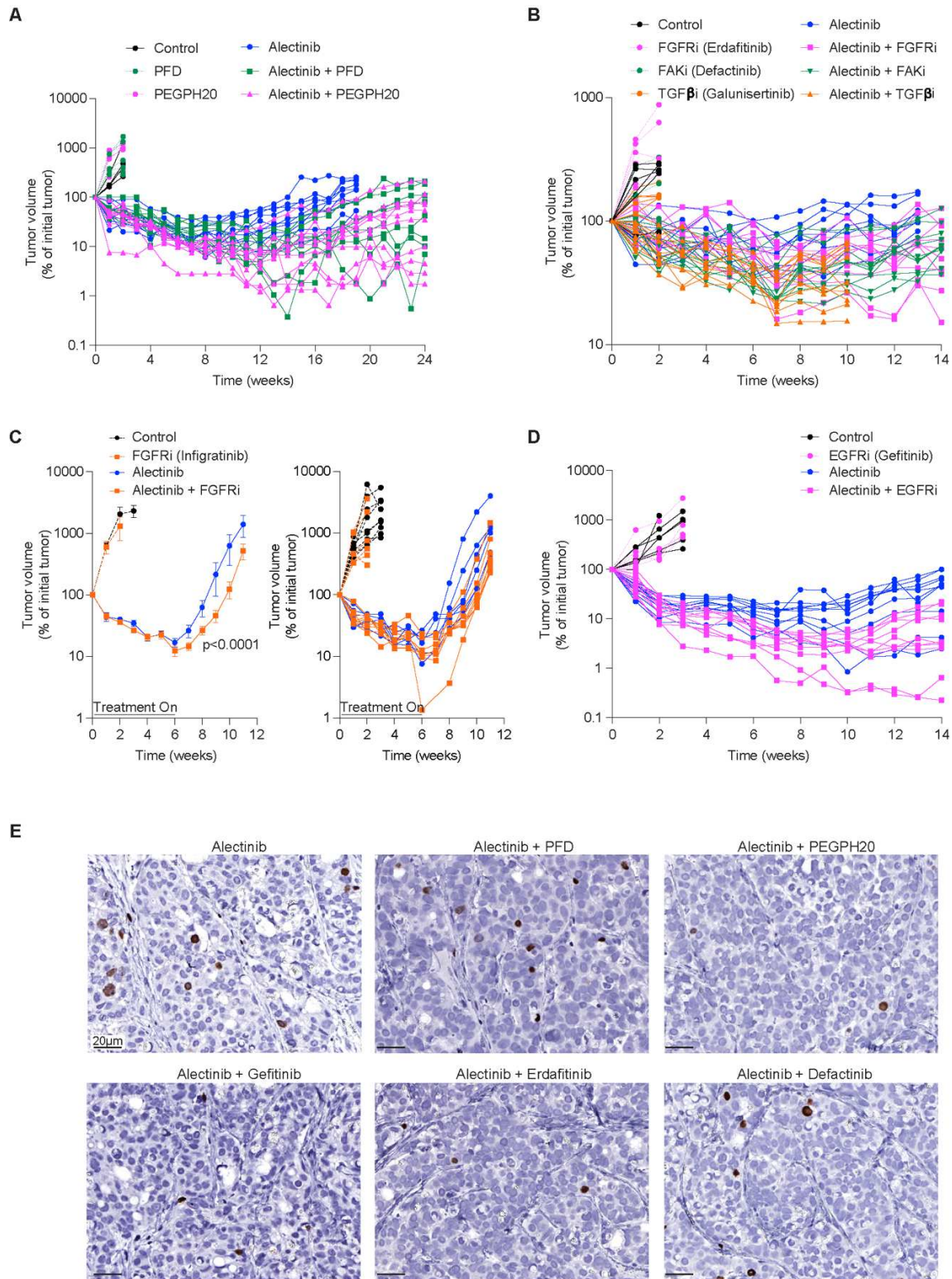
Figure S6

Figure S6. (**A**) Non-supervised hierarchical clustering of the gene expression heatmaps of differentially expressed genes in the indicated samples. (**B**) Volumetric responses of average (upper panel) and individual tumor traces (lower panel) of H3122 xenograft tumors in NSG hosts treated with vehicle control (N=4), 25mg/kg alpelisib (N=6), 25 mg/kg alectinib (N=8) and alectinib/alpelisib combination (N=10). Error bars represent SEM. P values represents the significance of the interaction term of 2-way ANOVA analyses between the alectinib and alectinib/alpelisib combination treated group. (**C**) Representative images of Mason Trichrome staining of the indicated tumors. (**D**) Representative images of the HABP IHC staining of the indicated tumors. (**E**) Heatmaps of expression of the indicated genes in the indicated experimental tumors.

Figure S7

A

STE-1

Control   Collagen coated   Fibronectin coated

B

H3122

C

Control NRG1 TGFα HBEGF BTC EREG EGF HGF FGF1 FGF2 FGF9 FGF18 IGF1

Control BMP4 BMP6 BMP7 TGFβ1 TGFβ2 Act A IL11 IGF2 IL6 AREG FGF10 FGF7

Figure S7. (**A**) Images of crystal violet staining of the clonogenic assay of STE1 cells cultured for 20 days in regular, collagen, or fibronectin-coated plates in the presence of DMSO control, 0.1 µM alectinib, and 0.5 µM crizotinib. (**B**) Cell viability assay for H3122 cells grown in the presence of the indicated factors (50 ng/ml). (**C**) Images of crystal violet staining of the 10 days culture of H3122 cells in the presence of the indicated growth factors (50 ng/ml).

Figure S8

Figure S8. (**A**) Volumetric traces of individual H3122 xenograft tumors treated with vehicle control, 900 mg/kg pirfenidone, 0.1mg/kg PEGPH, 25 mg/kg alectinib, alectinib/pirfenidone and alectinib/PEGPH20 combinations. (**B**) Volumetric traces of individual H3122 xenograft tumors treated with vehicle control, 20 mg/kg erdafitinib, 50 mg/kg defactinib, 75 mg/kg galunisertib, 20 mg/kg alectinib and the indicated combinations. (**C**) Volumetric traces of averages (left) and individual tumors (right) of H3122 xenograft tumors treated with vehicle control (N=10), 30 mg/kg infigratinib (N=6), 20 mg/kg alectinib (N=6), and alectinib/infigratinib combination (N=8). All mice received treatment break post 6 weeks. Error bars represent SEM. (**D**) Volumetric traces of individual tumors of H3122 xenograft tumors treated with vehicle control, 40 mg/kg gefitinib, 20 mg/kg alectinib and alectinib/gefitinib combination. (**E**) Representative images of anti-BrdU IHC staining of tumors tissues from H3122 xenograft mice treated with the indicated therapies for 7 days.
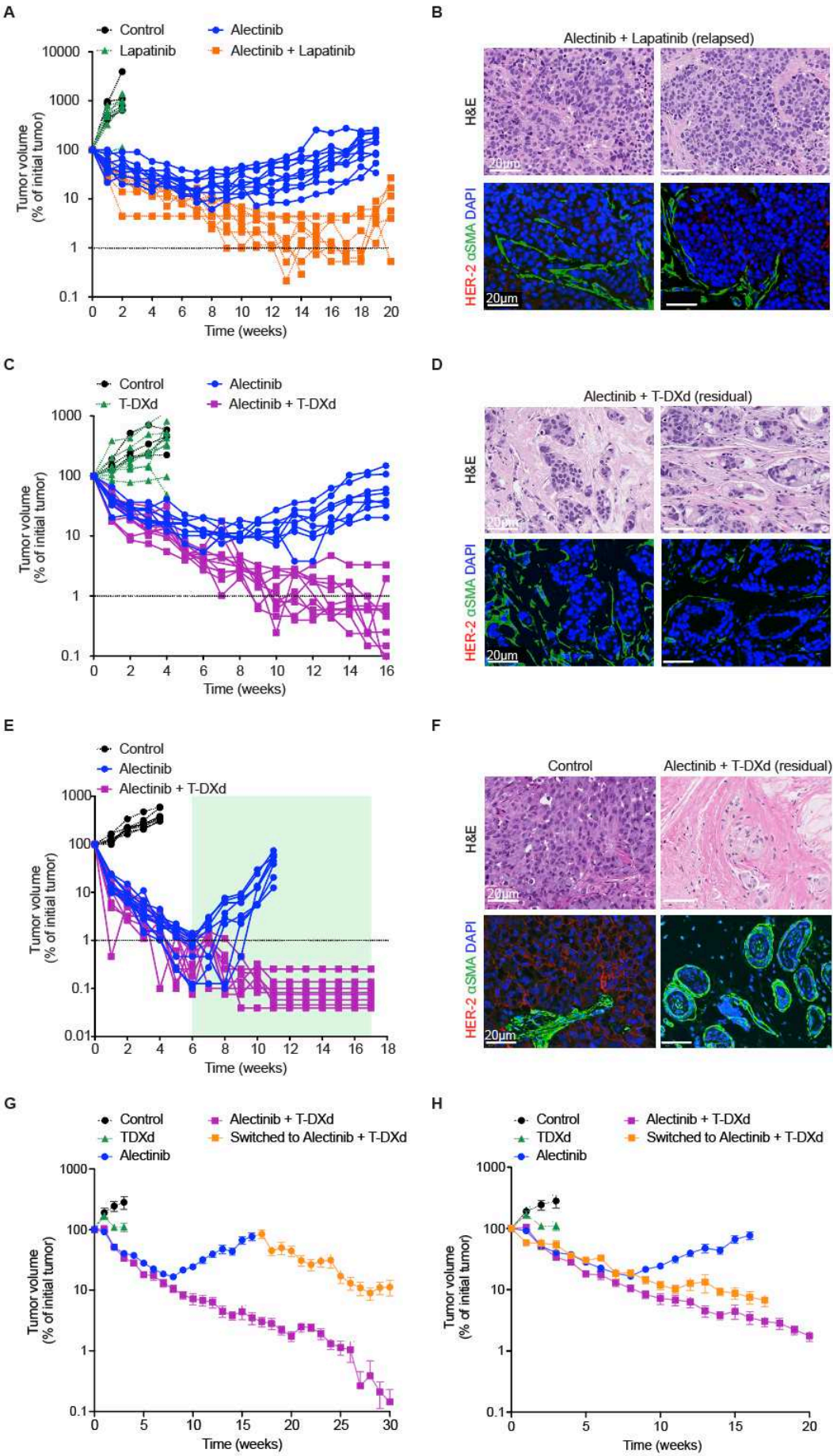
Figure S9
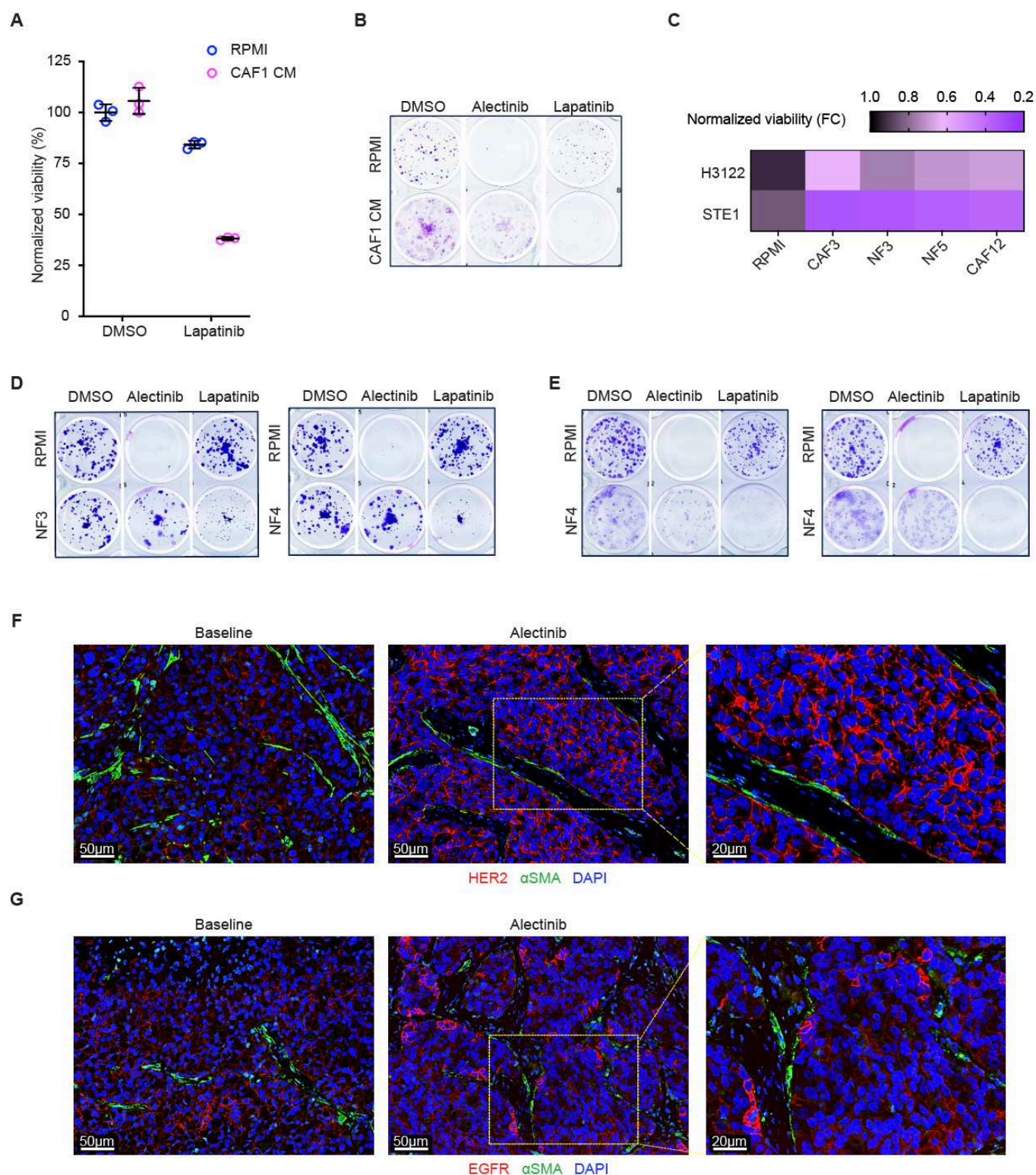
Figure S9. (**A**) Impact of CAF1 CM on sensitivity of STE-1 cells to 10 μM lapatinib in 4 days CellTiter-Glo assay. (**B**) Impact of CAF1 CM on sensitivity of STE-1cells to 0.1 μM alectinib and 10 μM lapatinib in 10 days Crystal Violet clonogenic assay. (**C**) Heatmap summary of the fibroblast CM induced lapatinib (10 μM) sensitization in H3122 and STE-1 cells. The sensitivity is presented as the fold change in cell viability as compared to the RMPI media control. (**D, E**) Crystal violet stain of the 10-day culture of H3122 (D) and STE-1 (E) cells in RPMI, or fibroblast CM in 0.1 μM alectinib, 10 μM lapatinib and DMSO control. (**F, G**) Representative images of IF staining of the indicated H3122 xenograft tumors with HER-2 (red) and αSMA (green) (F), or EGFR (red), and αSMA (green) (G).

Figure S10

Figure S10. (**A**) Volumetric traces of individual H3122 xenograft tumors treated with vehicle control, 100 mg/kg lapatinib, 25 mg/kg alectinib, and alectinib/lapatinib combination. (**B**) Representative images of the indicated endpoint H3122 xenograft tumors from (A) stained with H&E (upper panel) and IF co-staining against HER-2 (red) and αSMA (green) (lower panel). (**C**) Volumetric traces of individual H3122 xenograft tumors treated with vehicle control, 10 mg/kg T-DXd, 25 mg/kg alectinib, or alectinib/T-DXd combination. (**D**) Representative images of the indicated endpoint H3122 xenograft tumors stained with H&E (upper panel) and IF co-staining against HER-2 (red) and αSMA (green), DAPI (blue) (lower panel). (**E**) Volumetric traces of individual STE1 xenograft tumors treated with vehicle control, 20 mg/kg T-DXd, 12.5 mg/kg alectinib, and alectinib/T-DXd combination. (**F**) Representative images of the indicated endpoint STE1 xenograft tumors stained with H&E (upper panel) and IF and IF co-staining against HER-2 (red) and αSMA (green) (lower panel). Dotted lines in A, C and E indicate detectability threshold for volumetric measurements. (**G, H**) Volumetric traces of averages of H3122 xenograft tumors treated with vehicle control (N=8), 10 mg/kg T-DXd (N=8), 25 mg/kg alectinib (N=10), or alectinib/T-DXd combination (N=10). The impact of combination therapy on volumetric responses of tumor relapsed on alectinib monotherapy is shown in (G) and re-normalized at the point of switching to combination therapy in (H).